Electronic Supplementary Material (ESI) for Energy & Environmental Science.

Supplementary Materials for

Efficient perovskite solar modules with an ultra-long processing window enabled by cooling stabilized intermediate phases

Zhi Wan[1,#], Bin Ding[2,#], Jie Su[3,#], Zhenhuang Su[4], Zhihao Li[1,5], Chunmei Jia[1], Zhe Jiang[1], Qianqian Qin[1], Meng Zhang[1], Jishan Shi[1], Haodong Wu[7], Chongyang Zhi[1], Fengwei Wang[1], Chuan Li[1], Liming Du[1], Chao Zhang[4], Yong Ding[2,6], Can Li[1], Xingyu Gao[4], Chuanxiao Xiao[7,8], Jingjing Chang[3,*], Mohammad Khaja Nazeeruddin[2,*], Zhen Li[1,*]

[#]These authors contributed equally to this work.

[*]Corresponding author: Jingjing Chang: jjingchang@xidian.edu.cn; Mohammad Khaja Nazeeruddin: mdkhaja.nazeeruddin@epfl.ch; Zhen Li: lizhen@nwpu.edu.cn

Materials and Methods

Materials

All reagents were used as received without any further purification, including SnO_2 colloid (tin(IV) oxide, 15% in H_2O colloidal dispersion, Alfa Aesar), PbI_2 (99.99%, TCI), FAI (99.99%, Greatcell solar), MACl (99.5%, Xi'an Polymer Light Technology), spiro-OMeTAD (99.85%, Advanced Election Technology Co., Ltd), bis(trifluoromethane)sulfonimide lithium salt (Li-TFSI, 99.5%, Xi'an Polymer Light Technology), 4-tert-butylpyridine (TBP, 99.9%, Xi'an Polymer Light Technology), phenethylammonium iodide (PEAI, Xi'an Polymer Light Technology), chlorobenzene (CB, 99.5%, Sigma-Aldrich), acetonitrile (ACN, 99.8%, Sigma-Aldrich), N-Methylpyrrolidone (NMP, 99.5%, Sigma-Aldrich), N,N-dimethylformamide (DMF, 99.8%, Sigma-Aldrich), dimethyl sulfoxide (DMSO, 99.9%, Sigma-Aldrich), isopropanol (IPA, 99.5%, Sigma-Aldrich).

Methods

Precursor solution preparation

Tin (IV) oxide colloid solution (15 wt%) was diluted within DI water (2.67%)[1]. To prepare the PbI_2 solution, 1.5 M PbI_2 powder was dissolved in 900 μL DMF and 100 μL DMSO for PbI_2@D/D precursor solution, and for PbI_2@D/N precursor solution, 1.5 M PbI_2 powder was dissolved in 900 μL DMF and 145 μL NMP, and then heated and stirred at 60°C for 2 hours in an N_2-filled glovebox to fully dissolve. For the preparation of the solution of organic amine salts, FAI 90 mg, MACl 9 mg dissolved in 1 mL isopropanol solution, stirred at room temperature until dissolved in an N_2-filled glovebox. The spiro-OMeTAD solution was prepared by dissolving 90.0 mg spiro-OMeTAD in 1 mL chlorobenzene, adding 23 μL Li-TFSI (from 520 mg ml^{-1} stock acetonitrile solution) and 10 μL FK209 (376 mg ml^{-1} stock acetonitrile solution) and 39.5 μL 4-tert-butylpyridine.

Small-size perovskite solar cell fabrication

The tin-doped indium oxide (ITO) substrates were washed by detergent, and cleaned ultrasonically in deionized water, acetone, absolute ethanol and isopropanol sequentially for 10 min. Then, the substrates were dried with N_2 flow, followed by UV-Ozone treatment for 10 min, and the substrate was spin-coated with a thin layer of SnO_2 nanoparticle film at 4000 rpm for 30 s, and annealed in ambient air at 150°C for 30 min[2]. The substrates were transferred to the ALD system (EPEALD-100A-DH) to deposit 5-10 cycles SnO_2 at low temperatures using precursors of tetrakis(dimethylamino) tin(iv) (99.9999%, KE-MICRO, Jiaxing) and deionized water. Then, the substrate with ultraviolet ozone for 15 min to improve the surface wetting and transfer to the N_2 glove box for subsequent processing. For $FAPbI_3$@D/N, the PbI_2@D/N precursor solution was prepared by spin-coating on ITO/SnO_2 at 1800 rpm for 30 s, followed by annealing in glovebox at 70°C for 1 min. After cooling to room temperature, the organic amine salt solution was spin-coated onto the PbI_2@D/N at 2000 rpm for 30 s, followed by thermal annealing at 150°C for 15 min in ambient air conditions (30-40% humidity) to form the $FAPbI_3$ perovskite thin films. For the PbI_2@D/D precursor solution was spin-coated on the ITO/SnO_2 substrates at 1500 rpm for 30 s in the N_2-filled glovebox, annealed at 70°C for 1 min. Then the organic amine salt solution was spin-coated on the PbI_2@D/D films at 2000 rpm for 30 s, and then subjected to a 150°C annealing for 15 min to form the $FAPbI_3$ perovskite films in ambient air condition. For passivation layer, the ammonium salt solution was dissolved in IPA with 20 mM and spin-coated on the surface of perovskite film at 5000 rpm for 30 s, without any further processing[3]. Then the hole transporting layer was deposited on top of the perovskite layer by spin-coating the spiro-OMeTAD solution at 2000 rpm for 30 s. Finally, the fabricated devices were deposited of 5 nm MoO_3 and 80 nm Au or 100 nm Ag electrode under a base pressure of 4.0×10^{-4} Pa under vacuum.

Perovskite solar mini-module fabrication

5 cm × 5 cm and 6.5 cm × 7 cm perovskite solar modules with 6 and 8 sub-cells monolithic interconnected in series were fabricated on the FTO glass substrates (Asahi). With laser scribing system, the series-interconnection of the module was realized by P1, P2, and P3 lines. The FTO substrate was pre-patterned for P1 (a width of 40 μm) by means of 20 W laser power under a speed of 500 mm/s with a frequency of 40 kHz

and pulse width of 100 ns (laser wavelength of 1064 nm). The FTO substrates with P1 were washed by detergent, and cleaned ultrasonically in deionized water, acetone, absolute ethanol and isopropanol sequentially for 10 min. The following steps were the same as the fabrication of small-area PSCs except the volume of the precursor. For $FAPbI_3$@D/N, the PbI_2@D/N precursor solution was prepared by spin-coating on ITO/SnO_2 at 1800 rpm for 30 s, followed by annealing in glovebox at 70°C for 1 min. After cooling to room temperature, the organic amine salt solution was spin-coated onto the PbI_2@D/N at 2000 rpm for 30 s, followed by thermal annealing at 150°C for 15 min in ambient air conditions (30-40% humidity) to form the large-area $FAPbI_3$ films. The n-Octylammonium lodide (OAI) post-treatment was applied to the perovskite films of large-area devices to reduce hysteresis. OAI solution (5 mg/mL in IPA) was spin-coated on the perovskite films, followed by 3 min annealing at 100°C. After the hole transporting layer was deposited on top of the perovskite layer by spin-coating the spiro-OMeTAD solution at 2000 rpm for 30 s, the samples were P2 scribed using green light (532 nm) with an average laser power of 2.5 W under a speed of 1000 mm/s and frequency of 40 kHz for pulse duration of 80 ns. Finally, the sample was thermally evaporated to deposit an Au electrode of approximately 80 nm, followed by P3 scoring using green light (532 nm) in precisely specified areas. For the anti-reflection coating, 150 nm magnesium fluoride (MgF_2) was electron-beam vapor deposited at an evaporation rate of 0.5-2.5 Å s^{-1}. The detailed processing parameters of the nanosecond laser (Zhongneng Photoelectric, PSH130-L20-S400-D-B57-S3, Hangzhou) for P1, P2, and P3 the width of the scratch is shown in Fig. S40. The width of the interconnection area is about 200 μm. The width of a single sub-cell (including dead area) is about 6.6 mm. The geometrical FF (GFF) can be calculated as 97.0%.

Characterization

The photovoltaic device performances were measured by using 2400 Series Source Meter (Keithley Instruments) under AM 1.5 G 100 mW cm^{-2} simulated solar irradiation from a solar simulator (Newport 94063A Oriel Sol3A, Class AAA) calibrated using a Si standard cell with a KG-5 filter. To ensure the accuracy of the J_{SC} measured from *J*-

V scans, a mask with an aperture area of 0.045 cm^2 was covered during the measurement. For the small-size solar cells, the *J-V* curves were scanned by reverse (forward bias (1.2 V) to short circuit (-0.1 V)) or forward (short circuit (-0.1 V) to forward bias (1.2 V)) scan with scan rate of 0.1 mV s^{-1}, delay time of 1 ms, and voltage step of 50 mV. For the modules, the *J-V* scan range was from 0 to 9.45 V with scan rate of 100 mV s^{-1}. The metal mask with an aperture area of 16.8 cm^2 or 27.81 cm^2 was covered during the measurement. The whole test process was carried out in the N_2 glove box at room temperature. The external quantum efficiency (EQE) spectra were measured using a quantum efficiency measurement system (Enli Tech, QE-R 3011). The nucleation and crystallization process of perovskite was observed by light microscope (Leica DM2700 M). The surface morphologies of different perovskite films and the cross-sectional structure of the devices were investigated by Scanning electron microscopy (FEI Nova Nano SEM 450). The Proton nuclear magnetic resonance (NMR) spectra were measured with a nuclear magnetic resonance spectrometer (Bruker AVANCE III HD 500 MHz, Germany). Steady-state photoluminescence (PL) spectra were recorded on a FLS 980 (excitation wavelength: 480 nm) fluorescence spectrophotometer. The time resolved photoluminescence (TRPL) spectra were acquired using an Edinburgh Instruments FLS920. X-ray diffraction (Bruker D8 Discover), UV-vis spectra (Lambda 35, Perkin-Elmer) were used for the characterization of the perovskite films. Fourier transform infrared (FTIR) spectra were recorded in ATR mode (Thermo, Nicolet 6700). For Mott–Schottky analysis, capacitance–voltage measurements were carried out at a fixed frequency (10 kHz) (Energylab XM, PARSTAT 3000A DX). A Mott–Schottky plot was obtained in the forward direction from -0.2 V to 1.5 V. The active area of the counter electrode was calibrated to 0.045 cm^2. The TPV and TPC measurements were carried on a homemade system (the oscilloscope model is MDO3014 from Tektronix). The *in-situ* UV-vis spectra of the perovskite intermediate phases film were tested in ambient air and *in-situ* steady-state photoluminescence (PL) spectra were tested in N_2 using a homemade system with a spectrometer (QE Pro, Ocean Optics). The *in-situ* grazing-incidence wide-angle x-ray scattering (GIWAXS) experiment of perovskite intermediate phases film were measured in N_2 at BL14B1 beamline of the Shanghai

Synchrotron Radiation Facility (SSRF). The energy of the X-ray is 12.12 keV. The samples were measured at an incident angle of 1°. The photoluminescence images were obtained by the electro-photoluminescence Integrated Detection System (Suns-EPL-P500$^+$). Using bright blue LED excitation with excitation wavelength of 420-450 nm, and using 680 or 720 nm long pass filter to remove interference from blue LED, photoluminescence images were obtained with a 5-megapixel camera (MV-GEC501M#A9FEA0ED).

Stability measurement

Light stability testing

The operational stability of the best-performed PSCs at the maximum power point (MPP) conditions was studied on a solar cell stability test system (PURI2400-E8, PURI Materials) under 100 mW cm^{-2} illumination. The light source was supplied with a white LED lamp. The samples were tested in N_2 atmosphere with a surface temperature of about 45°C. It starts by applying the maximum voltage derived from the first *J-V* curve (Fig. 4h), then the applied voltage is perturbed every minute with a small voltage variation to search for the MPP, and the corresponding maximum voltage, maximum current and maximum power are recorded. For the MPPT test, the PEAI passivation layer was removed, because PEAI would gradually transform into PEA_2PbI_4 phase when the device was heated during the test, which brought into significantly efficiency drop and shorter lifetime[4]. To test the stability of the large area device (1.00 cm^2), we placed the device without any encapsulation in a N_2-filled glovebox for more than 2400 hours. For the stability test of the module, in order to inhibit the horizontal and vertical migration of I^-, after the scribing of P2, the thermal evaporation of MoO_x acted as a barrier layer. The stability of the module was subjected to continuous illumination under a white LED (100 mW cm^{-2}) and *J-V* test at regular intervals. The *J-V* curves were recorded with a Keithley 2400 source meter and under one sun illumination (AM 1.5 G, 100 mW cm^{-2}) equipped with solar simulator (Newport 94063A Oriel Sol3A, Class AAA) calibrated using a Si standard cell with a KG-5 filter.

Outdoor stability

The encapsulated 5 cm × 5 cm modules are placed on a homemade light platform with an angle of inclination of approximately 40°, facing due south. The temperature and humidity are tracked in real time by the high precision temperature and humidity recorder (COS-04) and powered by the silicon solar cell charging bank. The spectrum of natural light is recorded by the Ocean Optical spectrometer (WAVEGO-VIS-50). The periodic measurement of the *J*-*V* curve is done under the illumination of the solar simulator (Newport 94063A Oriel Sol3A, Class AAA).

Computational methods

The first-principles density functional theory (DFT) calculations on the basis of projector-augmented wave (PAW) method as implemented in the VAP code[5-7]. The Perdew-Burke-Ernzerhof (PBE) functional within the generalized gradient approximation was adopted to describe the exchange-correlation interaction[8]. DFT-D3 was employed to correct the van der Waals interaction[9]. The transformation barriers were calculated using the climbing image nudged elastic band (CI-NEB) method through the VTST tools[10,11]. The XRD peaks were calculated through the VESTA code. The plane-wave cut-off energy was set to be 400 eV. The convergence criterions for total energy and residual atomic forces were 10^{-5} eV/atom and 0.01 eV/Å, respectively. The self-consistent convergence accuracy was set at 10^{-7} eV/atom in the CI-NEB calculation. The Monkhorst-Pack k-point mesh in the Brillouin zone was set as to be Γ-centered with k-spacing of about 0.015 $Å^{-1}$. The perovskite and derivant models were constructed based on the Cambridge Crystallographic Data Centre and references[12-18], and then verified by the experimental XRD results. The numerical calculations in this paper have been done on the HPC system of Xidian University.

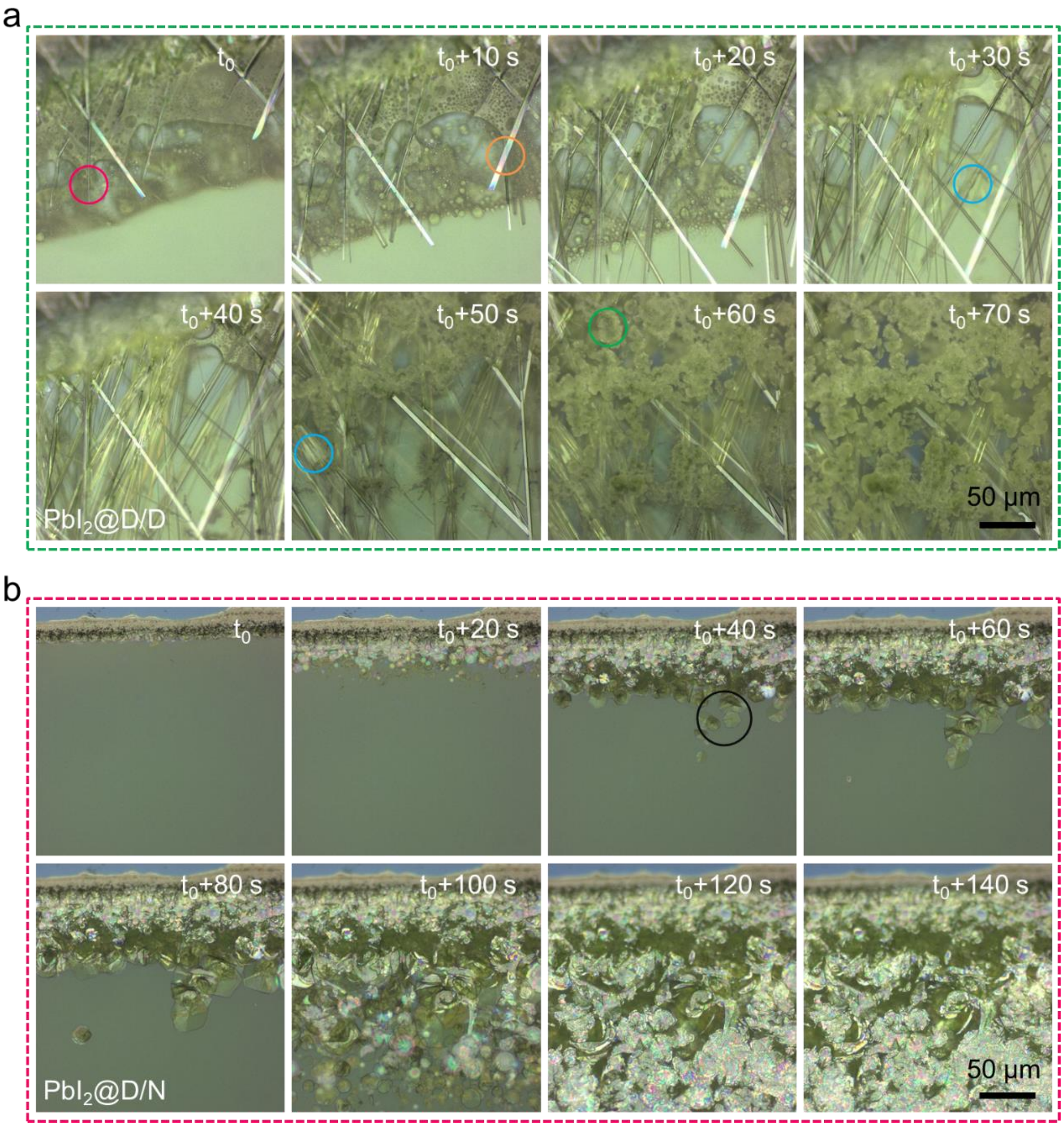

Fig. S1 Optical microscope photographs of PbI_2 nucleating from different solvent systems. (a) PbI_2@D/D. (b) PbI_2@D/N. In the D/D solution system, a variety of PbI_2 adducts were generated. At the beginning, a large number of needle-like PbI_2•DMSO crystals (red circle) were generated at the edge of the solution, followed by long and thick PbI_2•DMF crystals (orange circle) and thick dendritic PbI_2•2DMSO crystals (blue circle)[19-25]. Finally, with the evaporation of solvent, the solution was supersaturated and a large number of PbI_2 crystals (green circle) precipitated. Only lamellar PbI_2•NMP crystals (black circles) appeared in D/N solvent system, and single PbI_2 adducts were very conducive to subsequent perovskite nucleation and crystallization.

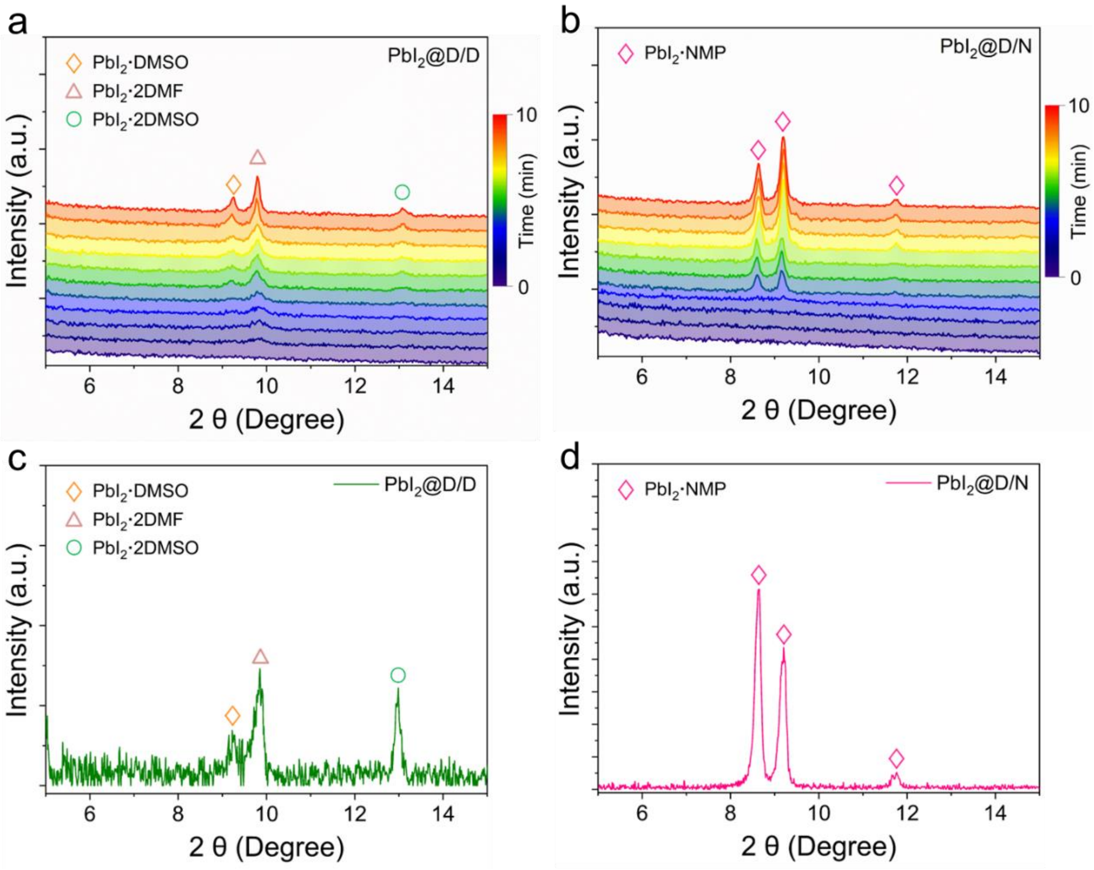

Fig. S2 *In-situ* XRD patterns of PbI_2 crystallized in different solvents. (a) PbI_2@D/D, (b) PbI_2@D/N. XRD patterns of PbI_2 films annealed at 70℃ for 1 min in different solvent systems. (c) PbI_2@D/D, (d) PbI_2@D/N.

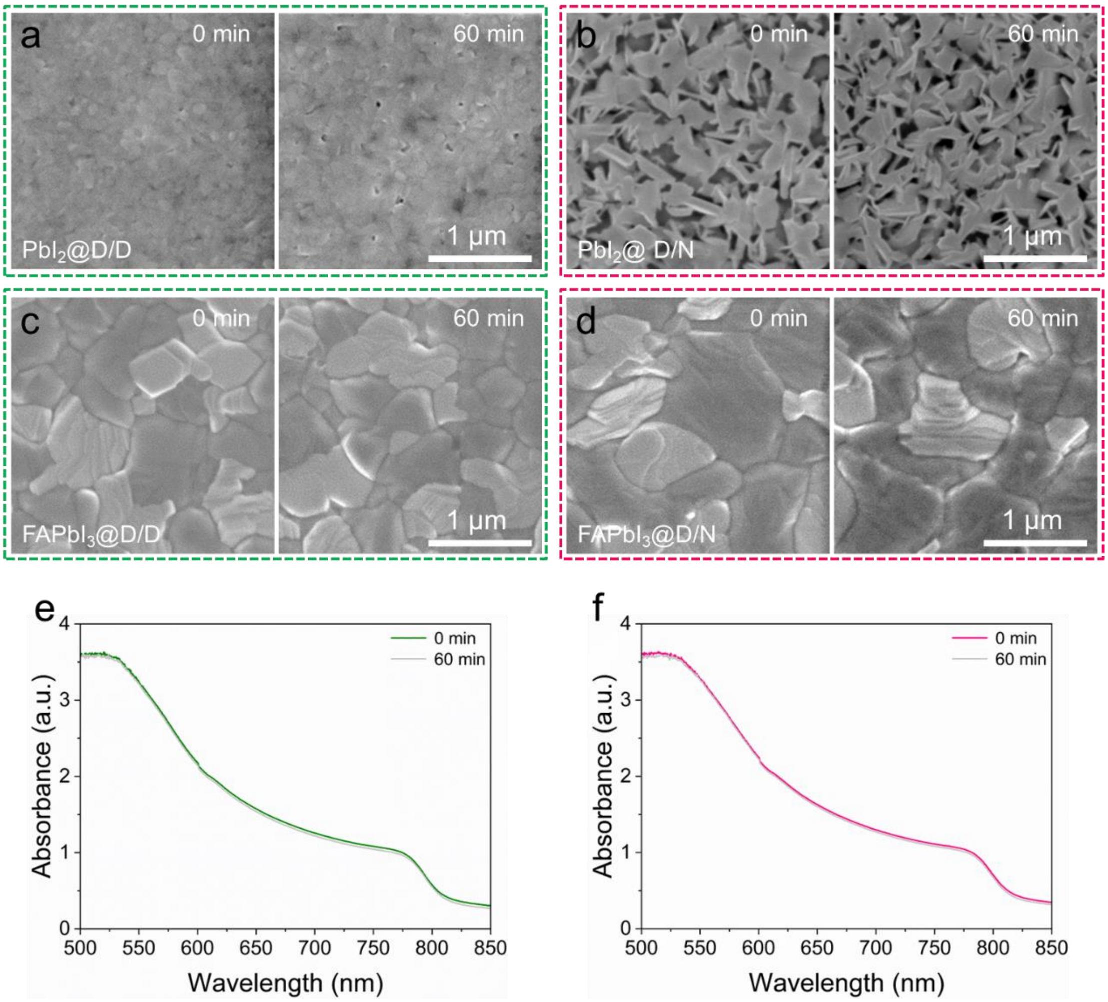

Fig. S3 The top-view SEM images of PbI_2 adducts fresh and aged for 60 min. (a) PbI_2@DMF/DMSO. (b) PbI_2@DMF/NMP. The corresponding SEM images of (c) $FAPbI_3$@D/D and (d) $FAPbI_3$@D/N perovskite films. UV-vis absorption spectrum of (e) $FAPbI_3$@D/D and (f) $FAPbI_3$@D/N perovskite films.

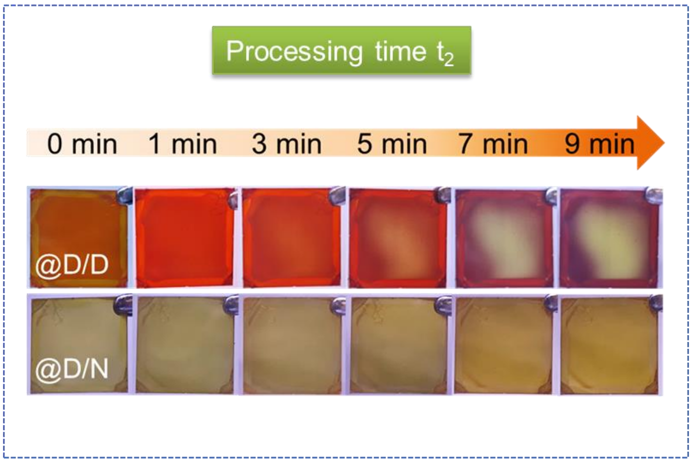

Fig. S4 Photos of perovskite intermediate phase evolution over time in D/D and D/N solvent systems.

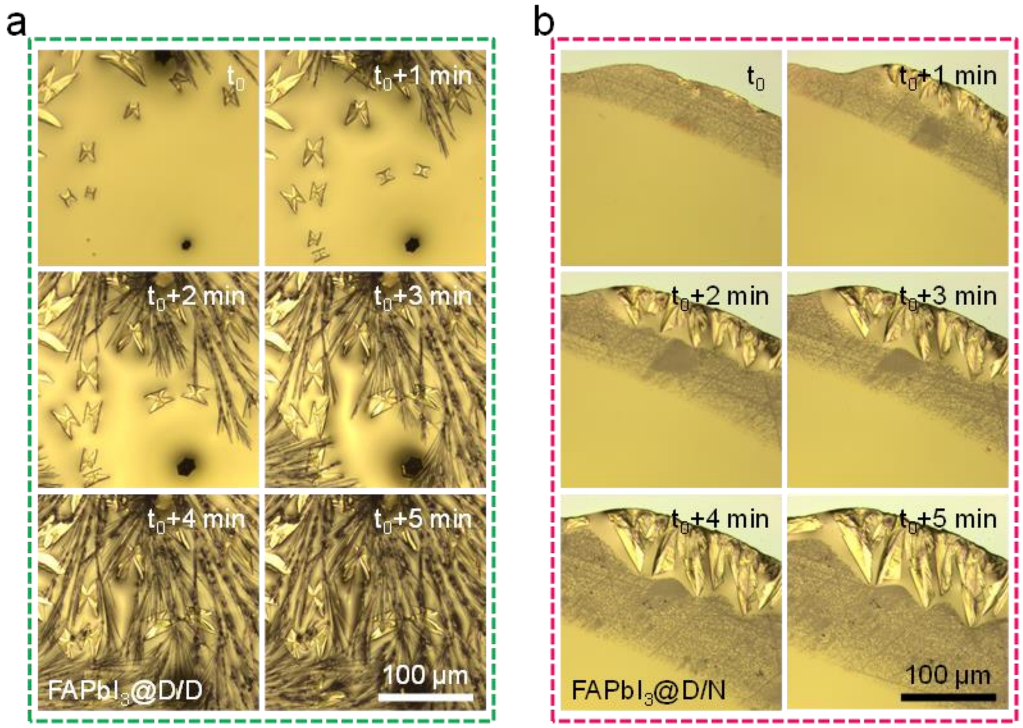

Fig. S5 Optical microscope photographs of $FAPbI_3$ perovskite nucleation crystallization process in different precursor solutions. (a) $FAPbI_3$@D/D. (b) $FAPbI_3$@D/N.

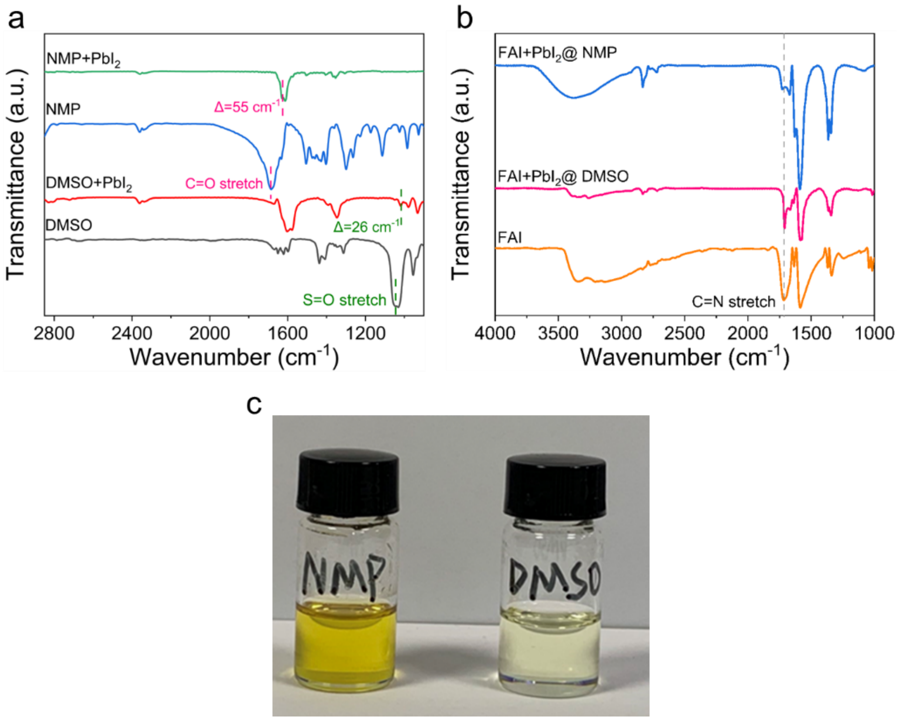

Fig. S6 (a) FTIR spectra of DMSO (solvent), NMP (solvent), DMSO/PbI$_2$ solution and NMP/PbI$_2$ solution. (b) FTIR spectra of FAI (powder), FAI + PbI$_2$@DMSO, and FAI + PbI$_2$@NMP perovskite intermediate phase. (c) The photos of FAI powder dissolved into DMSO and NMP. The solution solubility is 200 Mm[26].

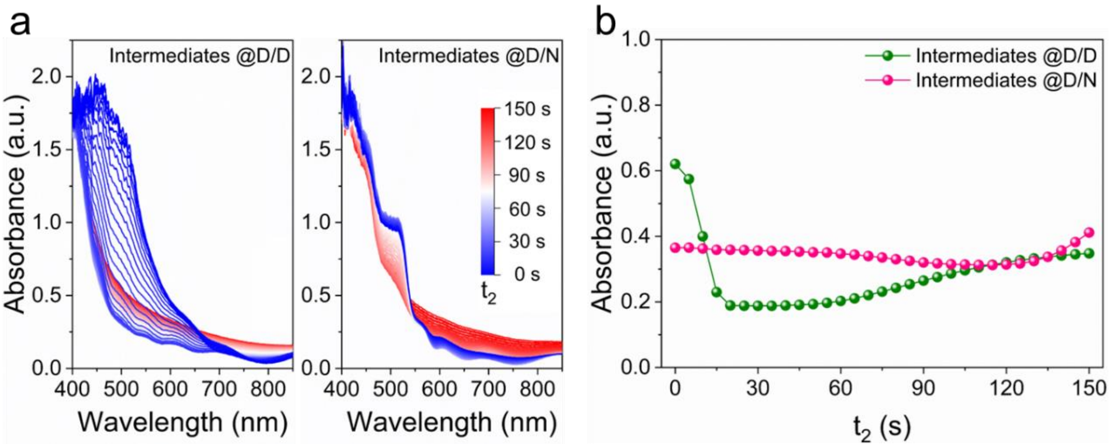

Fig. S7 *In-situ* UV-vis spectra of (a) intermediates@D/D and (b) intermediates@D/N wet film. (d) Average absorbance (from 450 nm to 800 nm) of intermediates@D/D and intermediates@D/N films as a function of time.

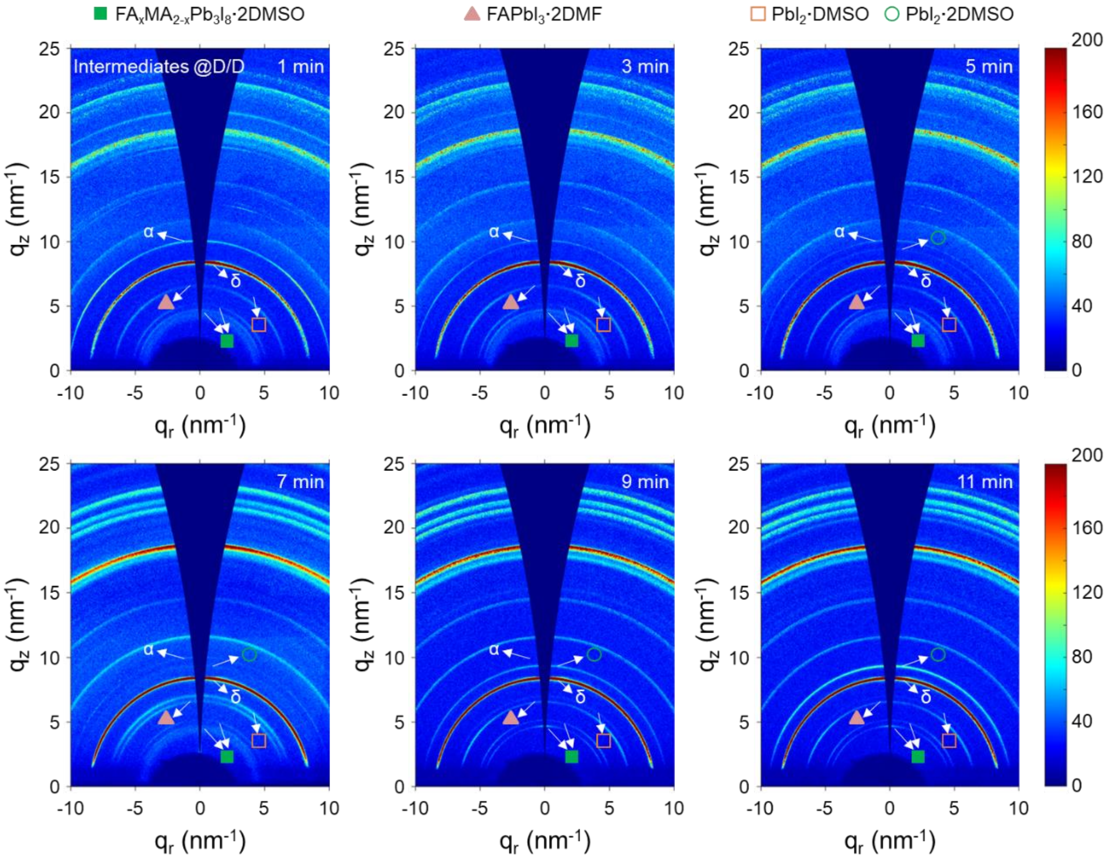

Fig. S8 2D GIWAXS patterns of intermediates@D/D films of different t_2.

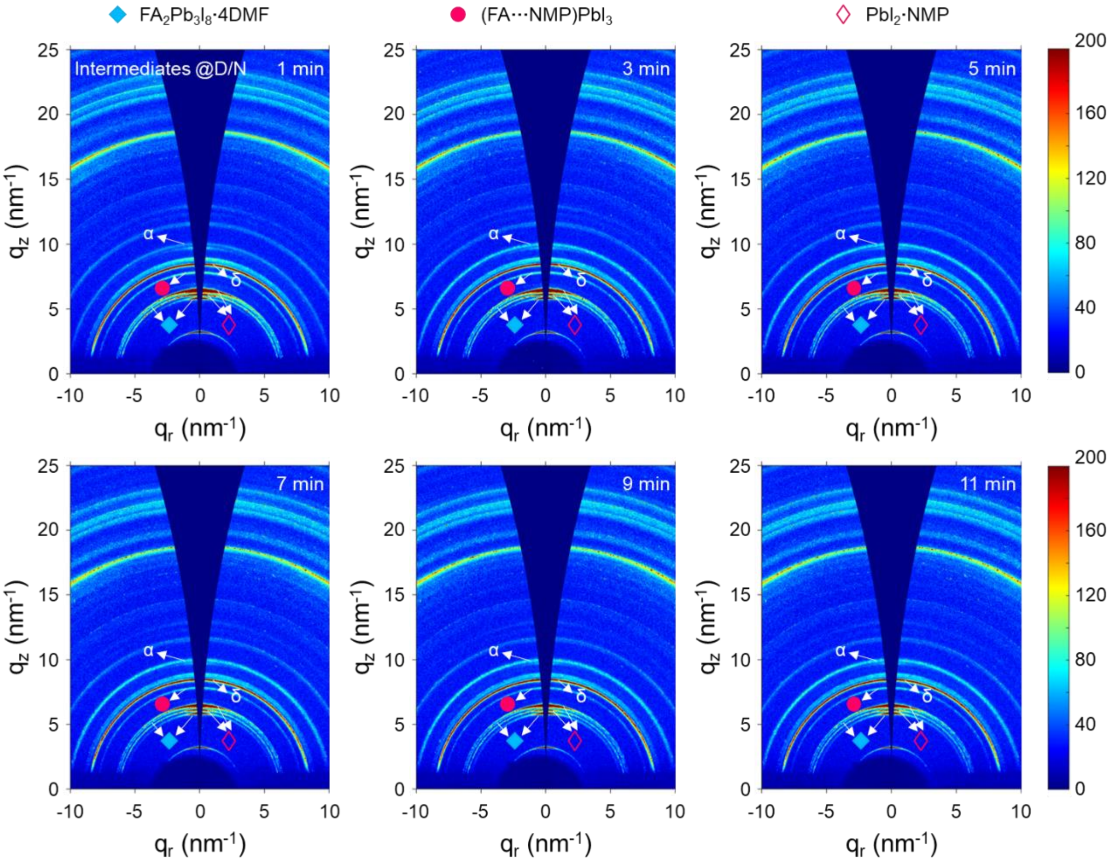

Fig. S9 2D GIWAXS patterns of intermediates@D/N films of different t_2.

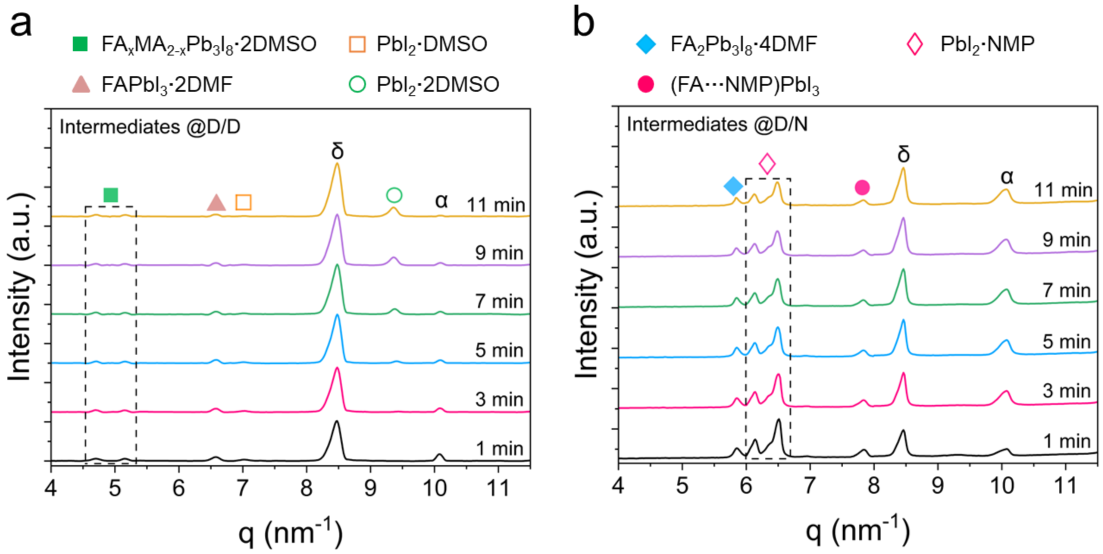

Fig. S10 1D GIWAXS integral spectra of (a) intermediates@D/D and (b) intermediates@D/N films of different t_2.

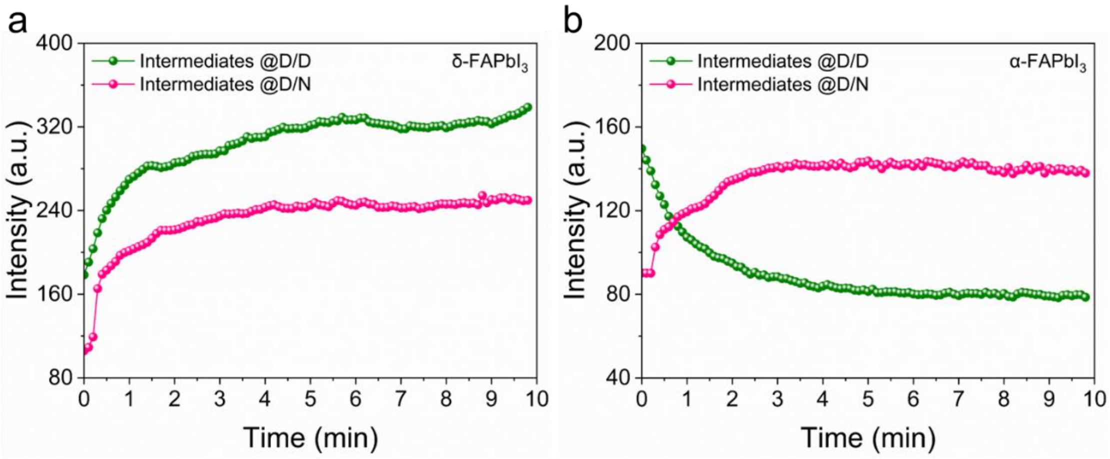

Fig. S11 The integrated intensity of δ-FAPbI3 phase (a)and α-FAPbI3 phase versus t_2 intermediate storage time, extracted from the *in-situ* GIWAXS results.

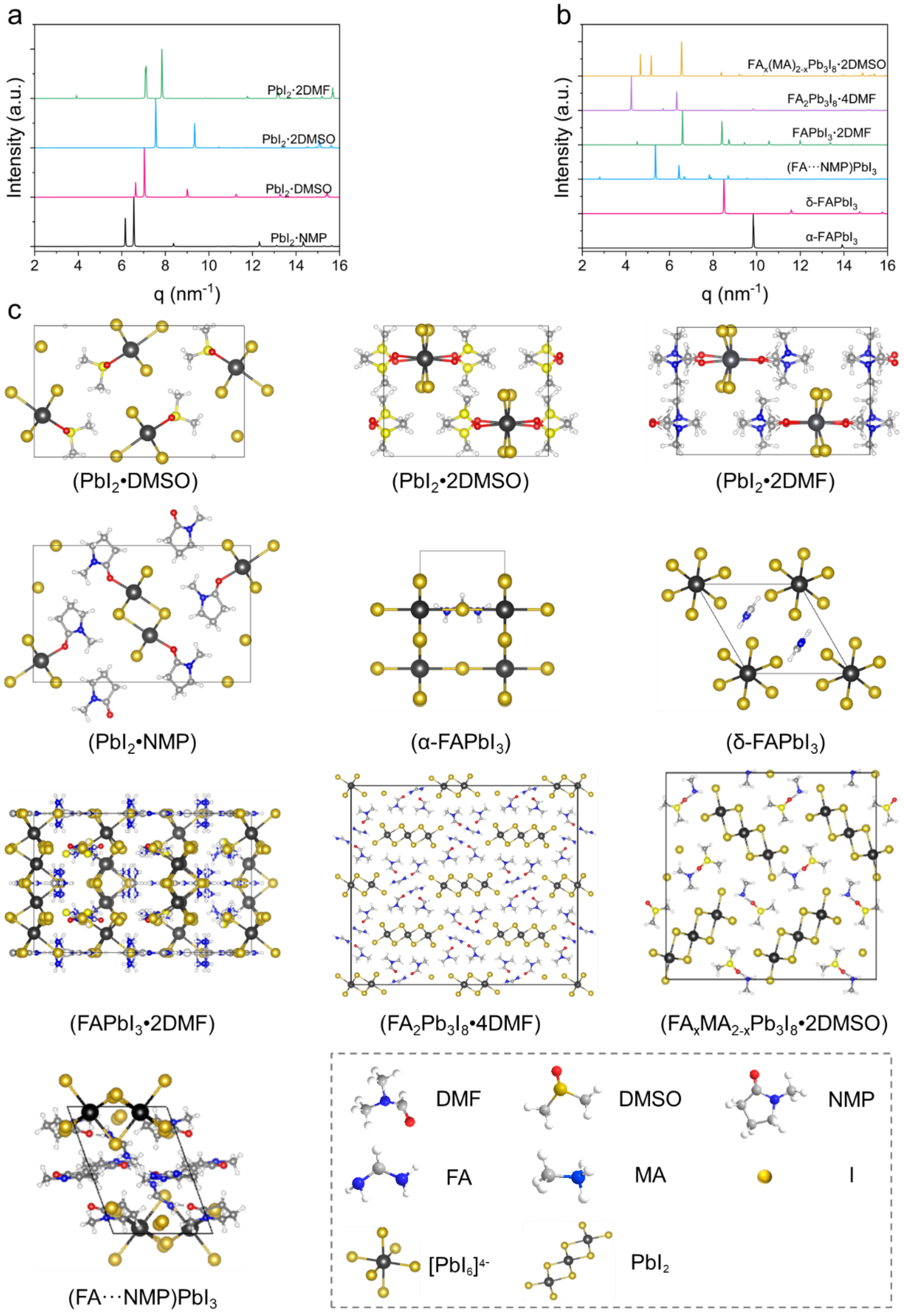

Fig. S12 DFT calculation of different perovskite components coordinated with different solvents. (a) PbI_2 adducts, and (b) $FAPbI_3$ intermediate phase. (c) The corresponding structures.

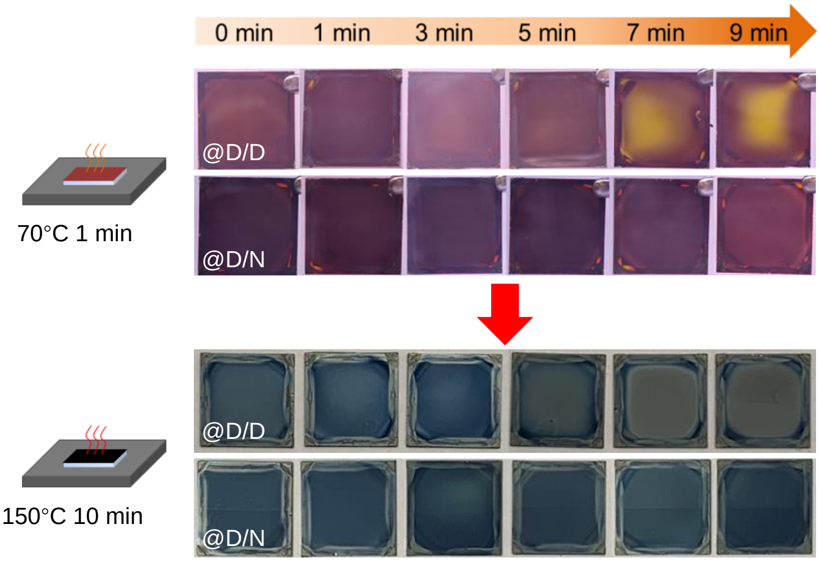

Fig. S13 Photos of the evolution of $FAPbI_3$@D/D and $FAPbI_3$@D/N films with t_2 at different annealing temperatures.

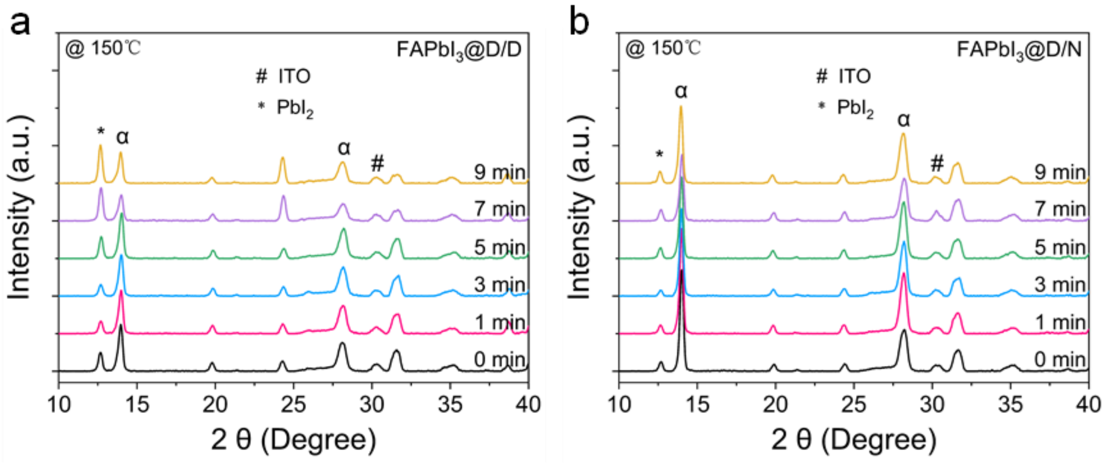

Fig. S14 XRD patterns of the FAPbI$_3$ films derived from intermediate films with different t_2 storage time: (a) FAPbI$_3$ from D/D intermediates; (b) FAPbI$_3$ from D/D intermediates.

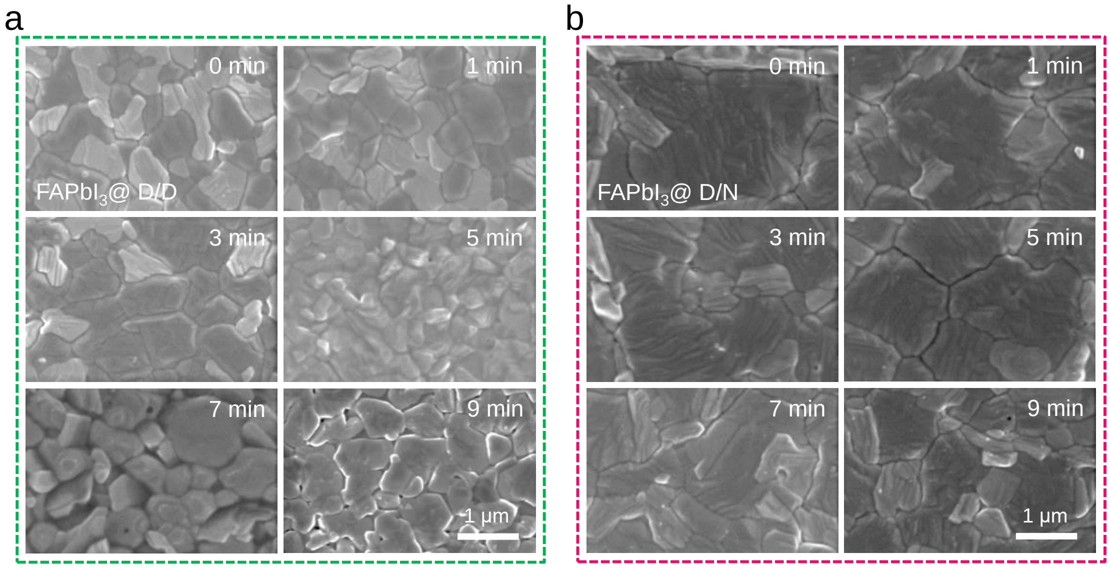

Fig. S15 SEM top-view images of the $FAPbI_3$ films derived from intermediate films with different t_2 storage time: (a) $FAPbI_3$ films from D/D intermediates; (b) $FAPbI_3$ films from D/D intermediates.

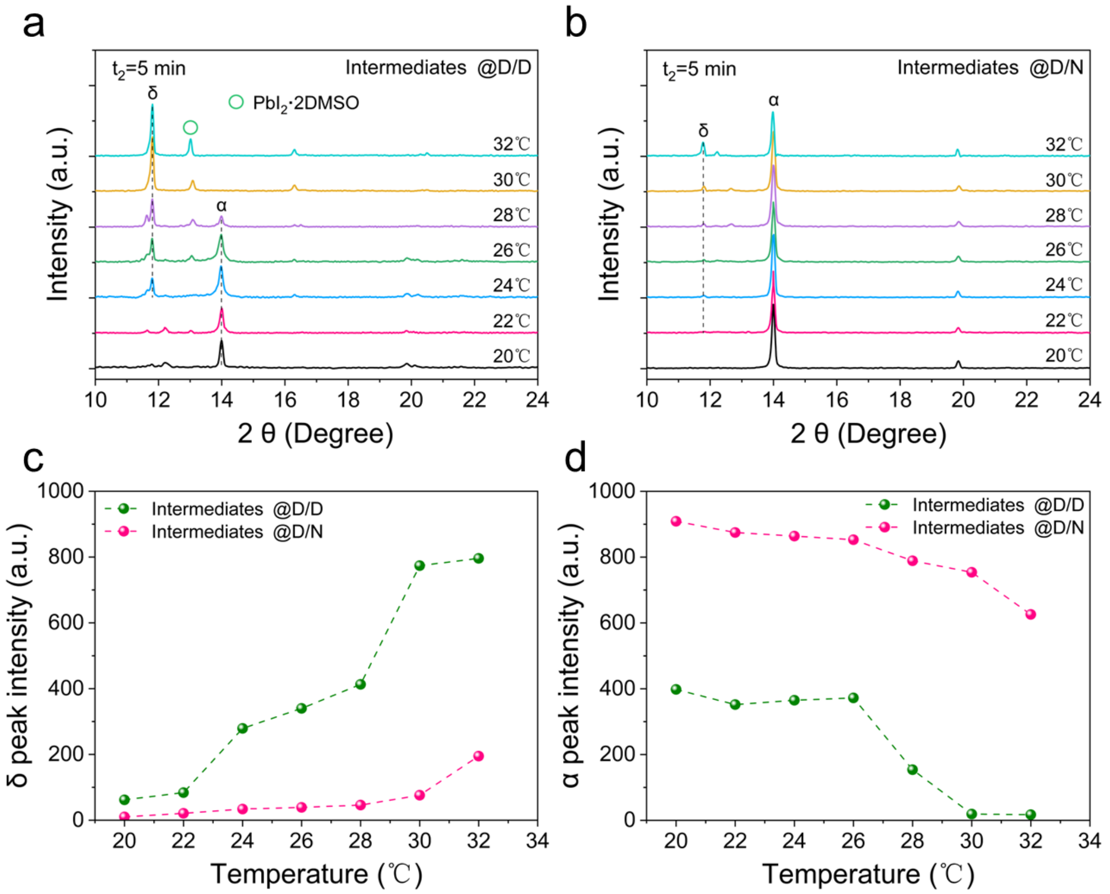

Fig. S16 XRD analysis of the intermediate films stored at different temperatures for 5 min: (a) XRD patterns of the intermediates from D/D solvents; (b) XRD patterns of the intermediates from D/N solvents; (c) the evolving of δ-phase peak area with increasing temperature; (d) the evolving of α-phase peak area with increasing temperature.

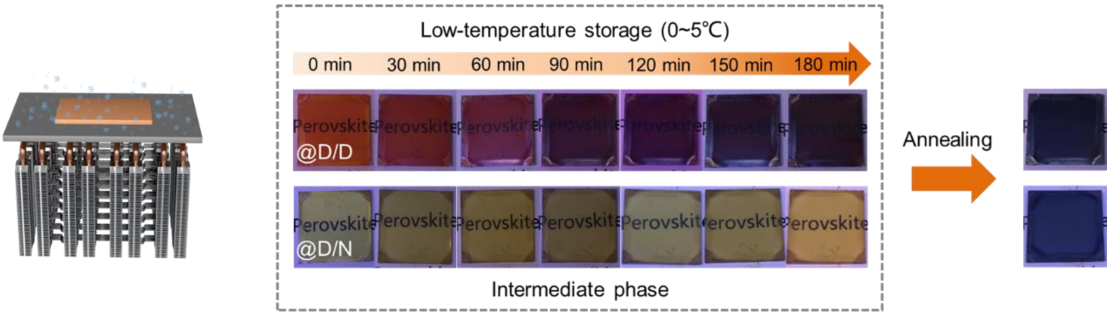

Fig. S17 Photographs of the evolution of perovskite intermediate phase films stored at low-temperature.

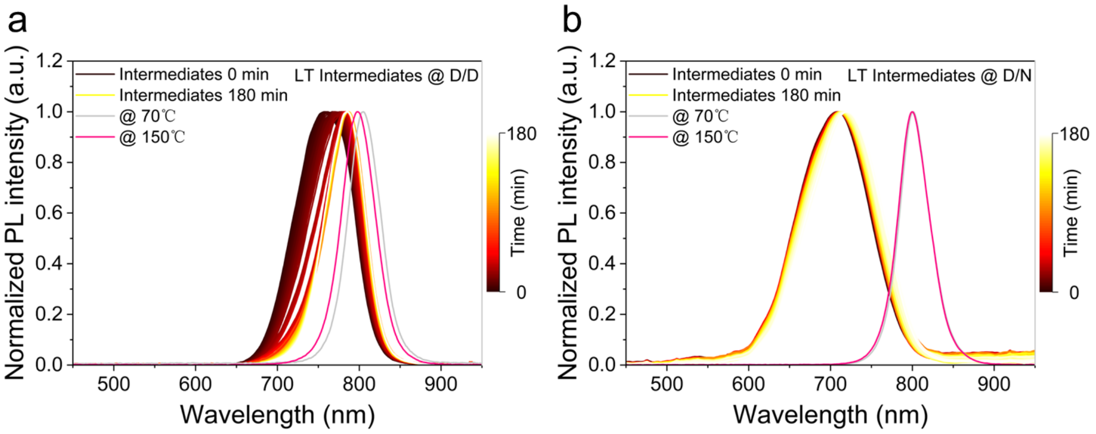

Fig. S18 *In-situ* PL spectra of (a) the intermediates@D/D and (b) the intermediates@D/N film with t_2 at LT (test in a nitrogen atmosphere).

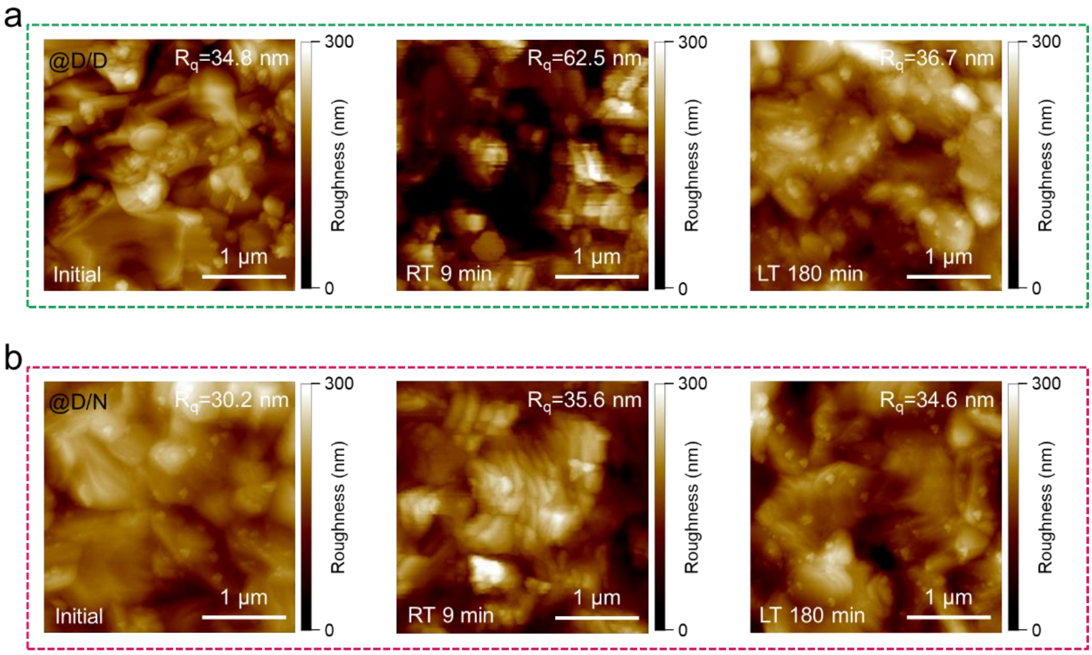

Fig. S19 AFM images of the perovskite films with different treatments. (a) $FAPbI_3$@D/D, (b) $FAPbI_3$@D/N.

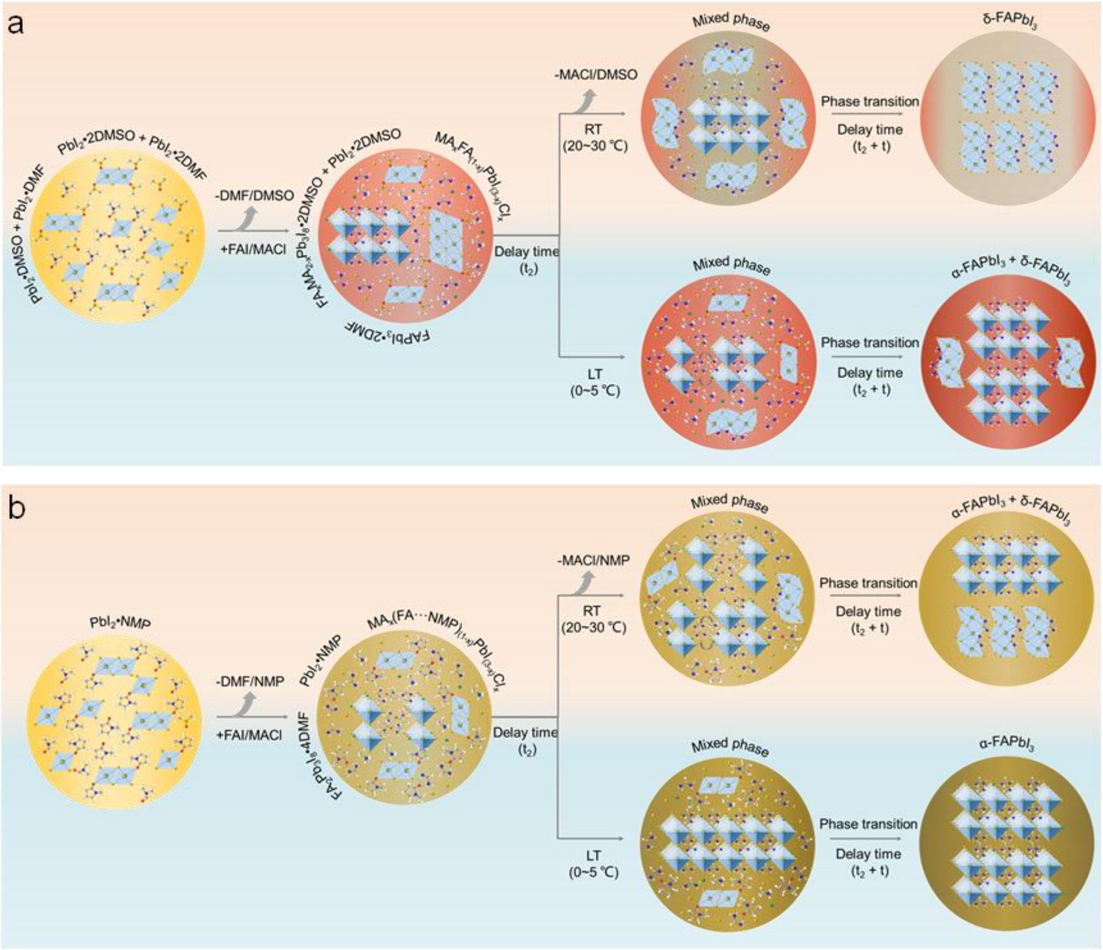

Fig. S20 The evolution scheme of (a) the intermediate @D/D and (b) intermediate @D/N at room temperature (RT) and low temperature (LT).

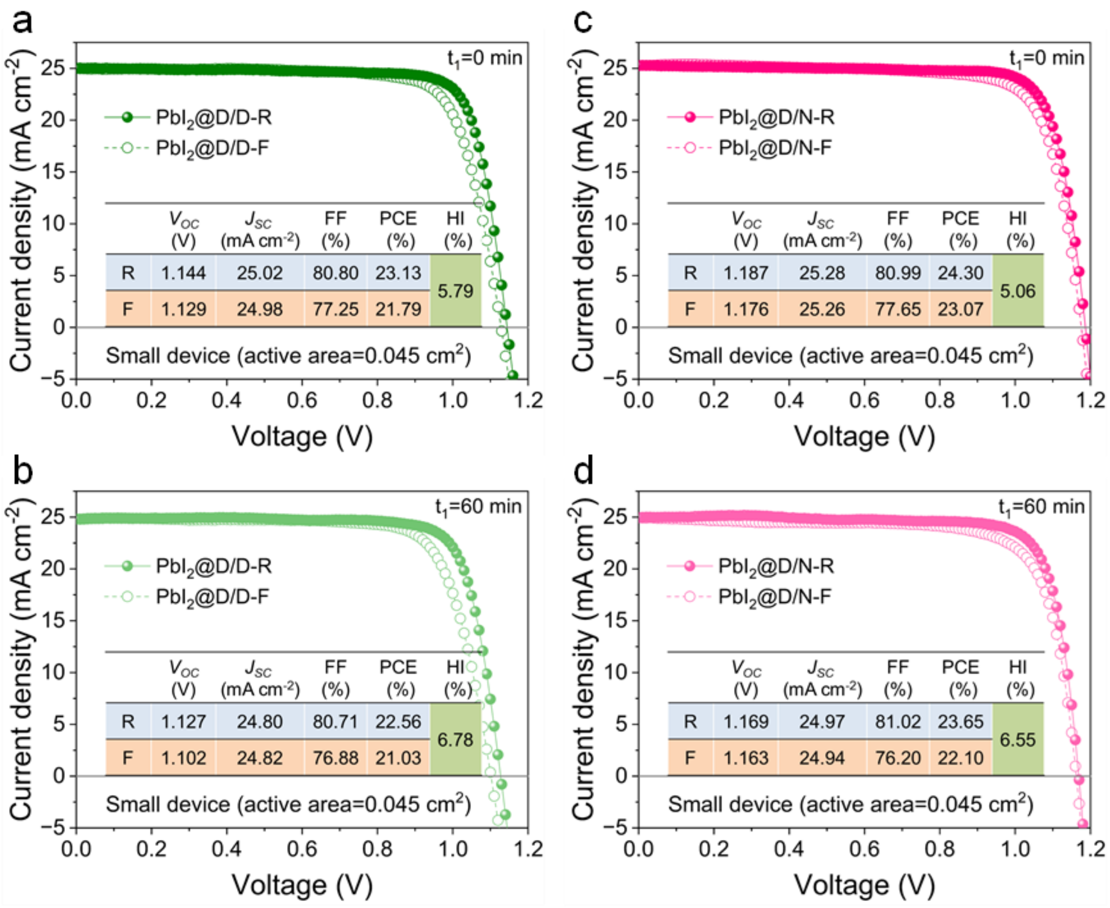

a

	V_{OC} (V)	J_{SC} (mA cm^{-2})	FF (%)	PCE (%)	HI (%)
R	1.144	25.02	80.80	23.13	5.79
F	1.129	24.98	77.25	21.79	

b

	V_{OC} (V)	J_{SC} (mA cm^{-2})	FF (%)	PCE (%)	HI (%)
R	1.127	24.80	80.71	22.56	6.78
F	1.102	24.82	76.88	21.03	

c

	V_{OC} (V)	J_{SC} (mA cm^{-2})	FF (%)	PCE (%)	HI (%)
R	1.187	25.28	80.99	24.30	5.06
F	1.176	25.26	77.65	23.07	

d

	V_{OC} (V)	J_{SC} (mA cm^{-2})	FF (%)	PCE (%)	HI (%)
R	1.169	24.97	81.02	23.65	6.55
F	1.163	24.94	76.20	22.10	

Fig. S21 Typical *J*-*V* curves of derived devices with PbI_2@D/D and PbI_2@D/N films stored at a humidity of approximately 20% ambient for different time: (a), (c) 0 min; (b), (d) 60 min.

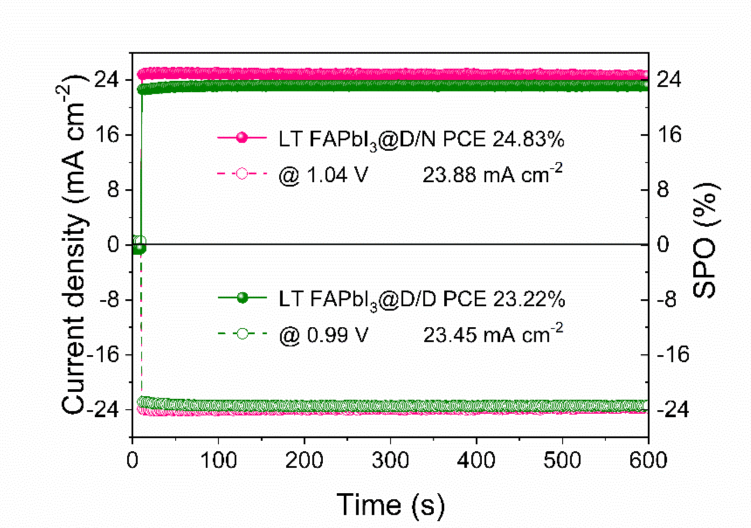

Fig. S22 Steady-state output at maximum power point (MPP) of LT FAPbI$_3$@D/D and LT FAPbI$_3$@D/N devices.

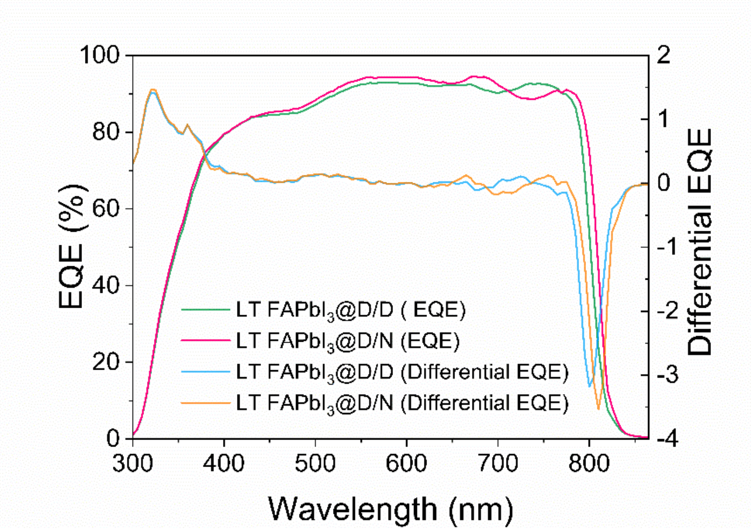

Fig. S23 EQE spectra of control and target PSCs.

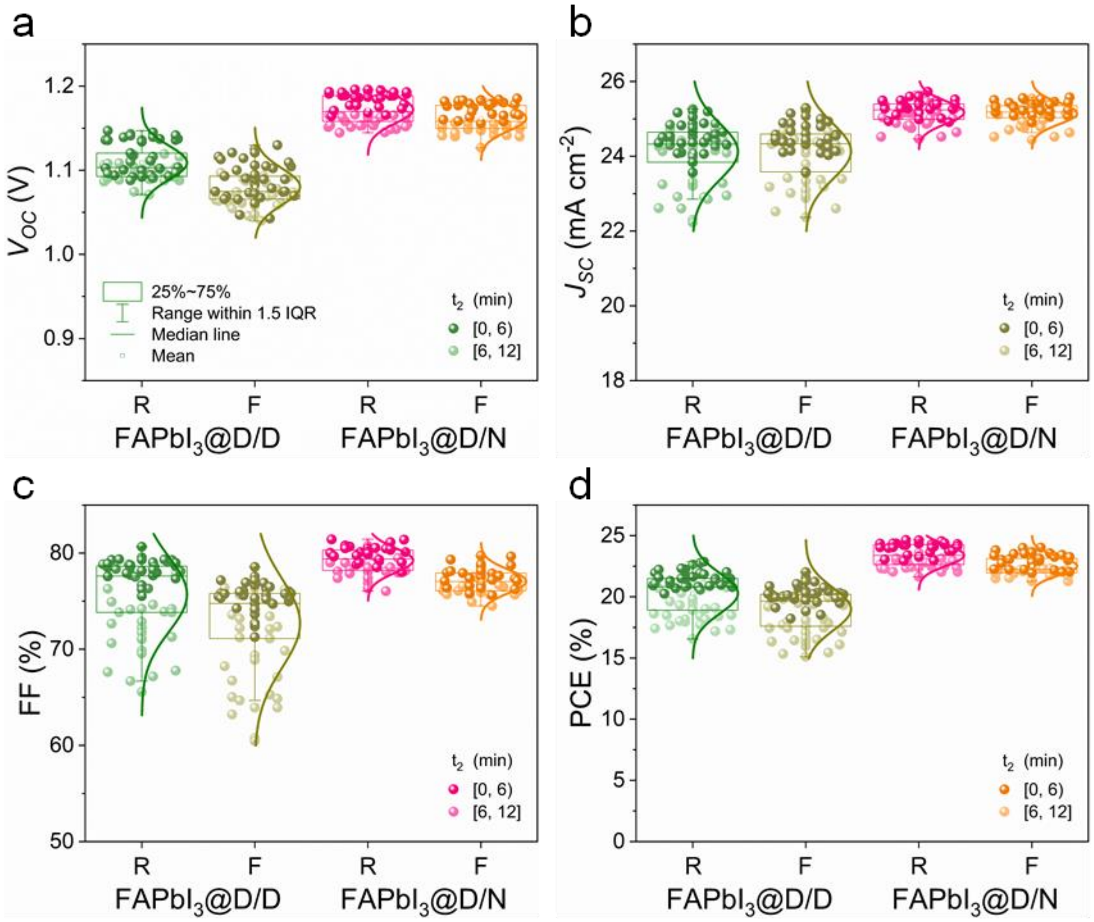

Fig. S24 Statistic distribution of photovoltaic parameters of two solvent systems derived devices. (a) V_{OC}, (b) J_{SC}, (c) FF, and (d) PCE statistics based on a total of over 48 individual perovskite solar cells, the waiting time t_2 of different perovskite intermediate phase films is within 12 min.

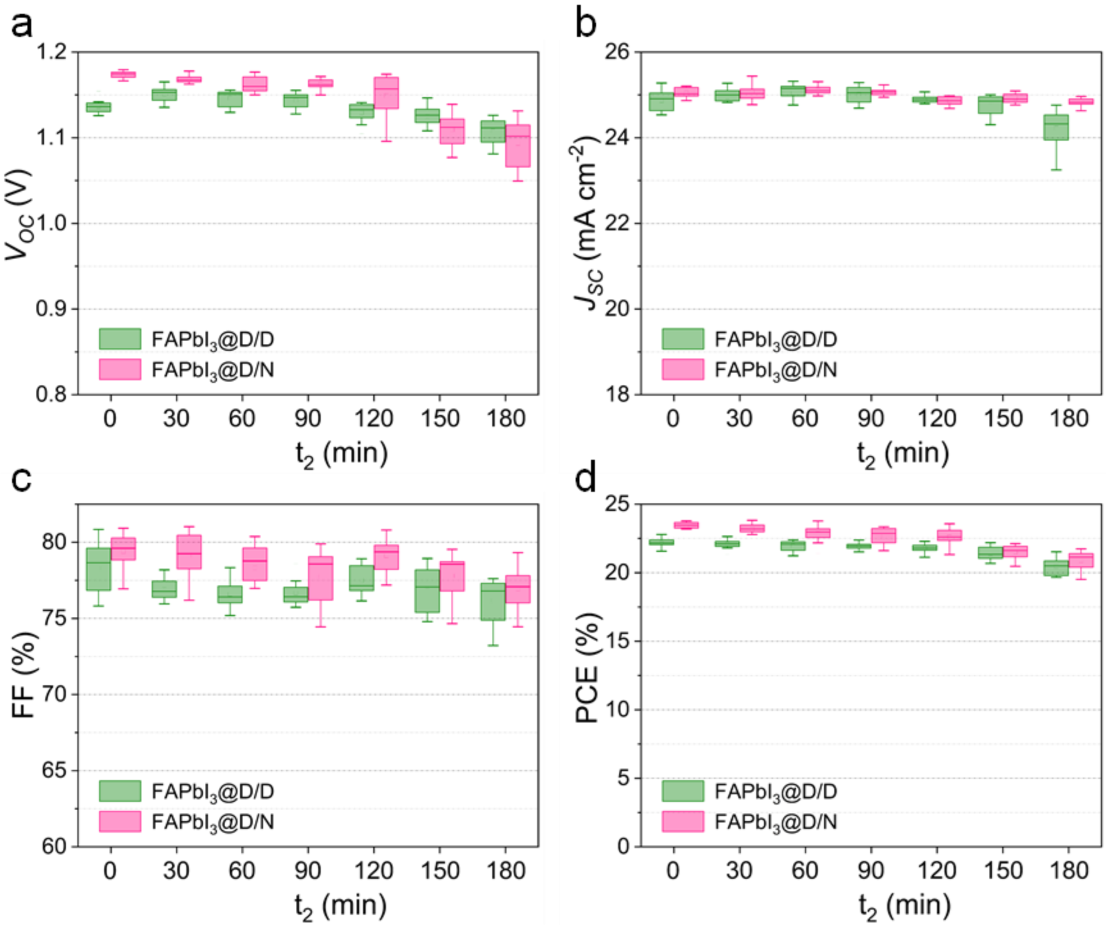

Fig. S25 Statistic distribution of photovoltaic parameters of two solvent systems derived devices with annealing delay time at LT. (a) V_{OC}, (b) J_{SC}, (c) FF, and (d) PCE statistics based on a total of 12 individual perovskite solar cells at corresponding waiting time t_2.

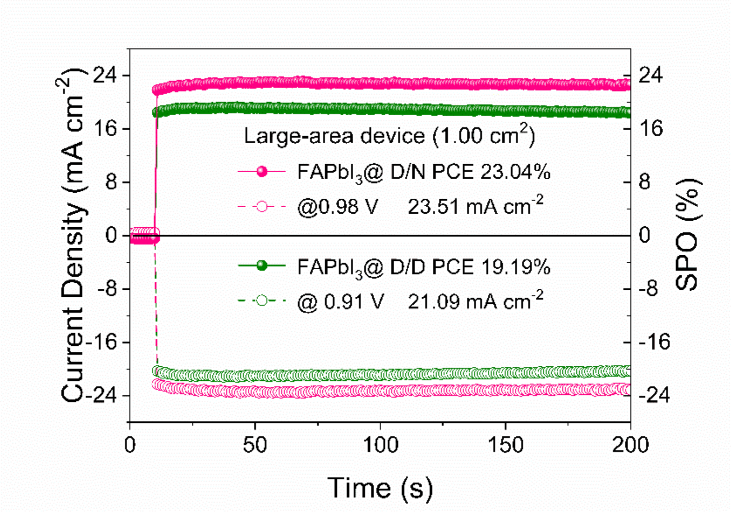

Fig. S26 Steady-state current densities and PCE tested at maximum power point for FAPbI$_3$@D/D and FAPbI$_3$@D/N devices (active area 1.00 cm^2).

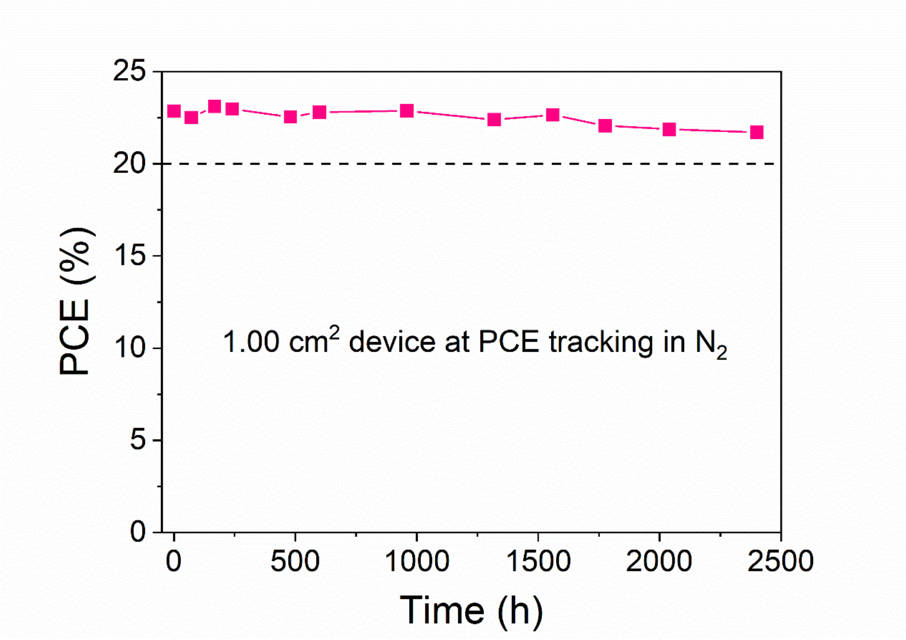

Fig. S27 Long-term stability of the large area FAPbI$_3$@D/N devices stored under dark nitrogen atmosphere.

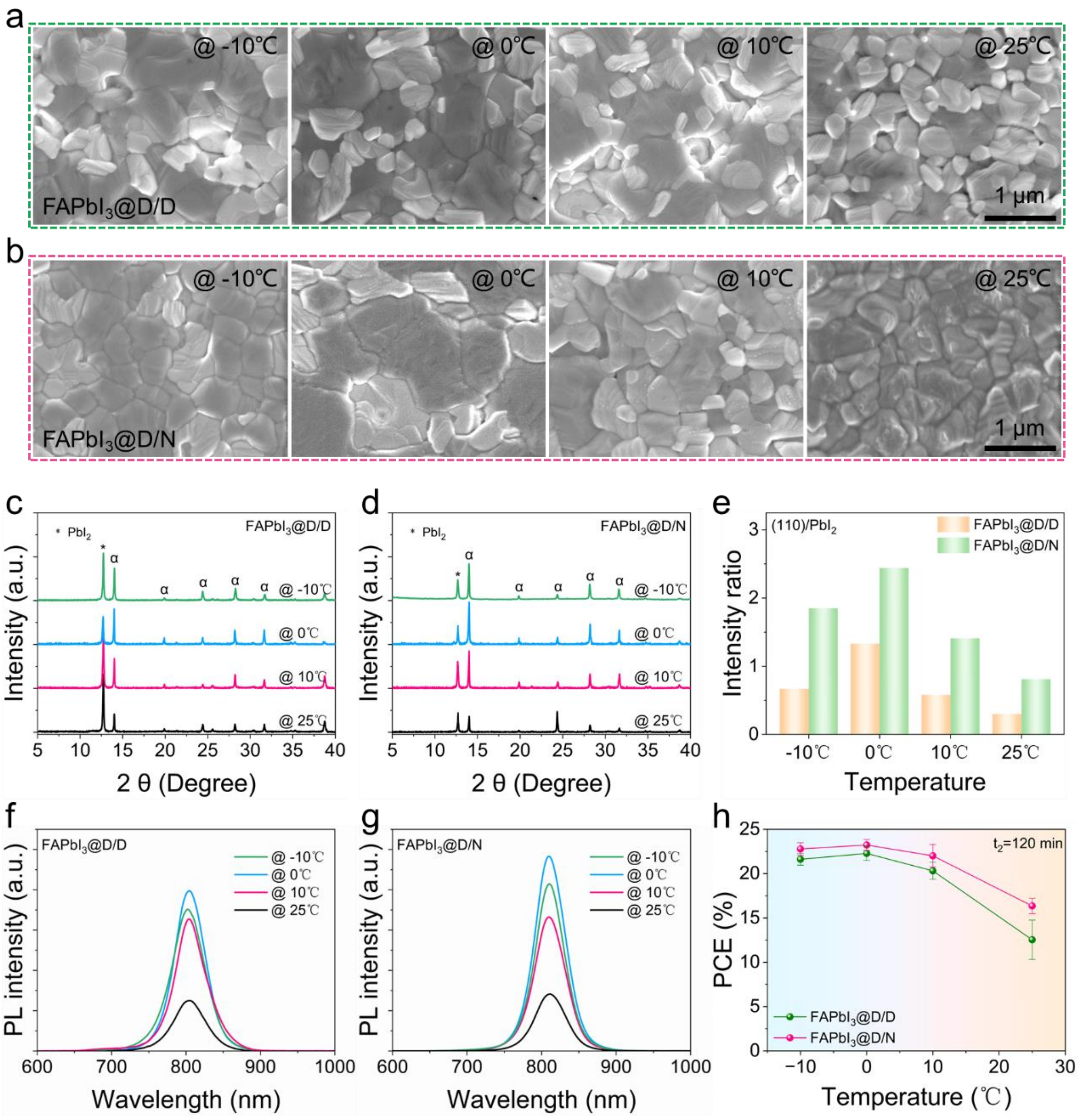

Fig. S28 Effect of annealing perovskite films treated at different temperatures for 120 min. Top-view SEM images of (a) FAPbI$_3$@D/D and (b) FAPbI$_3$@D/N. The XRD patterns of (c) FAPbI$_3$@D/D, (d) FAPbI$_3$@D/N films and (e) corresponding peak intensity ratio of perovskite (110) to PbI$_2$. PL spectra of (f) FAPbI$_3$@D/D and (g) FAPbI$_3$@D/N. (h) PCE changes in FAPbI$_3$@D/D and FAPbI$_3$@D/N film derived devices. Error bars were obtained from six separate cells.

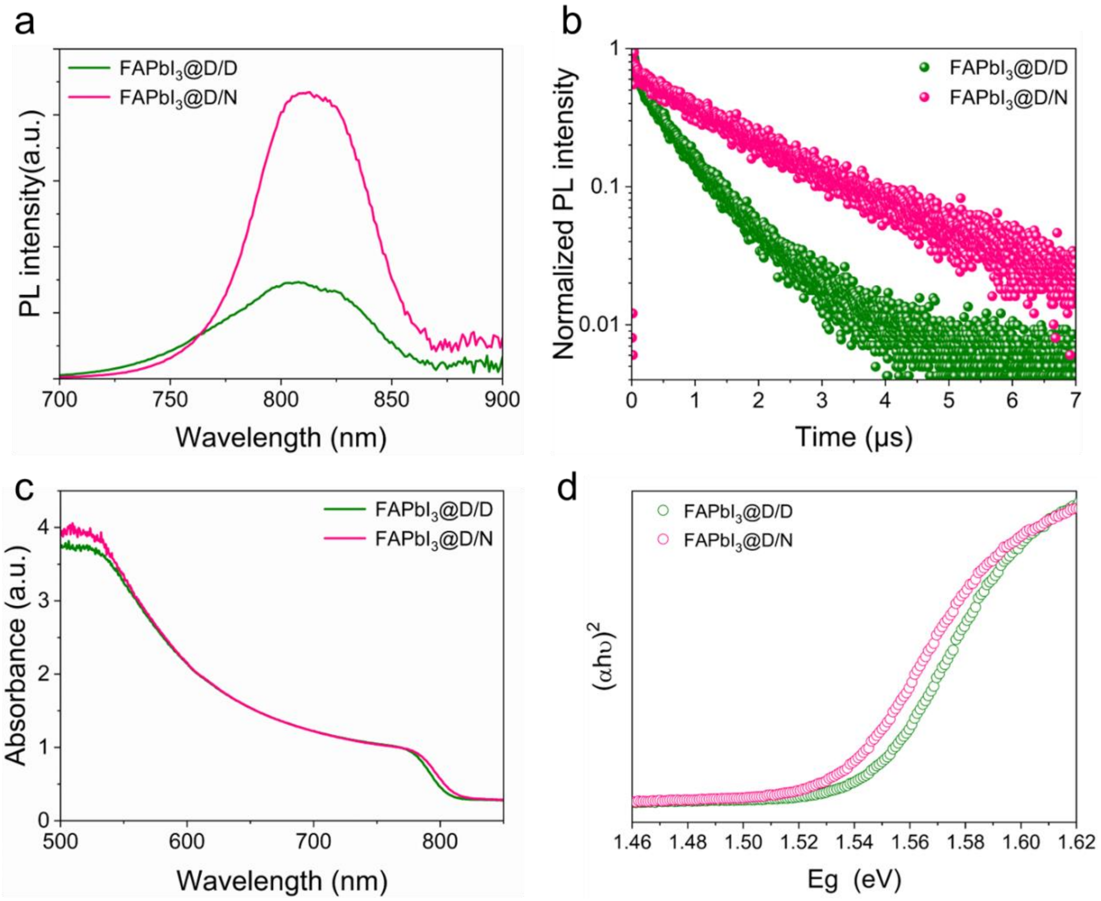

Fig. S29 (a) PL spectra of the $FAPbI_3$@D/D, $FAPbI_3$@D/N perovskite films. (b) TRPL spectra of $FAPbI_3$@D/D and $FAPbI_3$@D/N perovskite films (glass/perovskite). (c) UV-vis absorption spectra and (d) corresponding tauc plot of $FAPbI_3$@D/D and $FAPbI_3$@D/N perovskite films from the ultraviolet-visible absorption spectra[27].

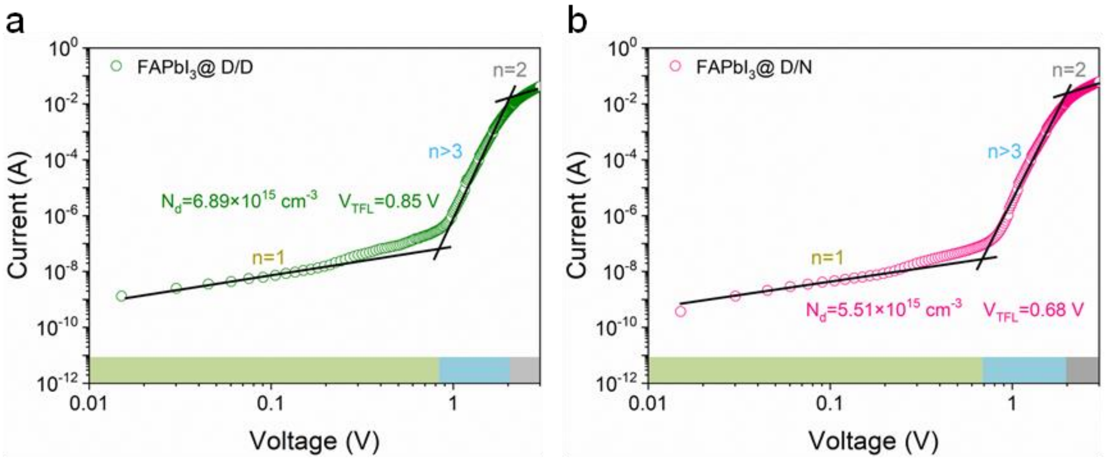

Fig. S30 *J-V* characteristics of (a) the $FAPbI_3$@D/D and (b) the $FAPbI_3$@D/N perovskite films derived from the SCLC measurements with a structure of ITO/perovskite/Au (ITO, indium tin oxide). V_{TFL}, trap-filled limited voltage. N_d, trap density[28]. The trap density is effectively decreased from 6.89×10^{15} cm^{-3} ($FAPbI_3$@D/D) to 5.51×10^{15} cm^{-3} ($FAPbI_3$@D/N).

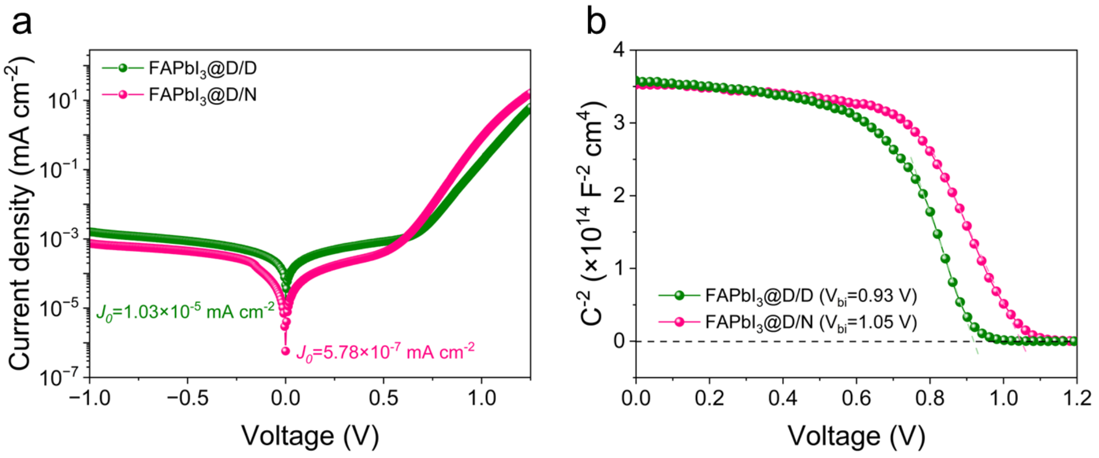

Fig. S31 (a) The dark *J*-*V* curves of $FAPbI_3$@D/D and $FAPbI_3$@D/N devices. (b) Mott-Schottky plot of $FAPbI_3$@D/D and $FAPbI_3$@D/N devices. The MS plot measurement conditions were determined to be a 10 kHz frequency based on the literature reports[29]. And then we fit this linear region to extract the built-in potential of PSCs.

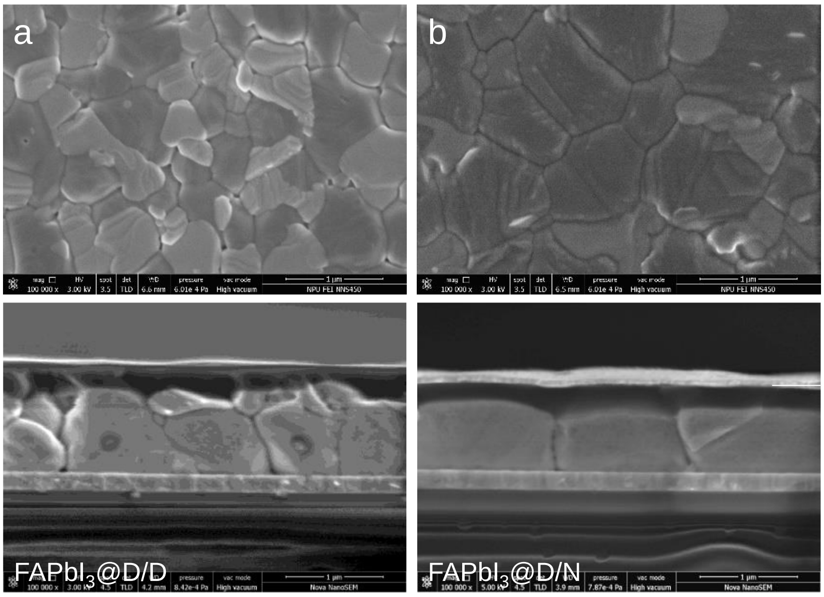

Fig. S32 Cross-sectional and top-view SEM images of (a) $FAPbI_3$@D/D and (b) $FAPbI_3$@D/N perovskite films.

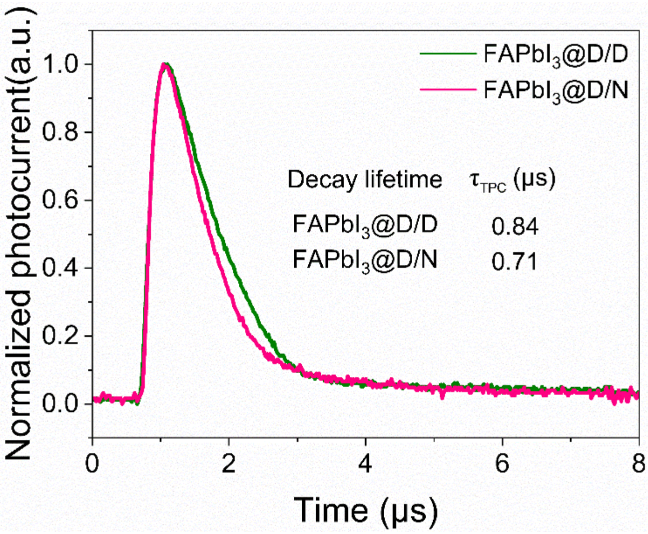

Fig. S33 TPC carrier recombination lifetime of FAPbI$_3$@D/D and FAPbI$_3$@D/N device.

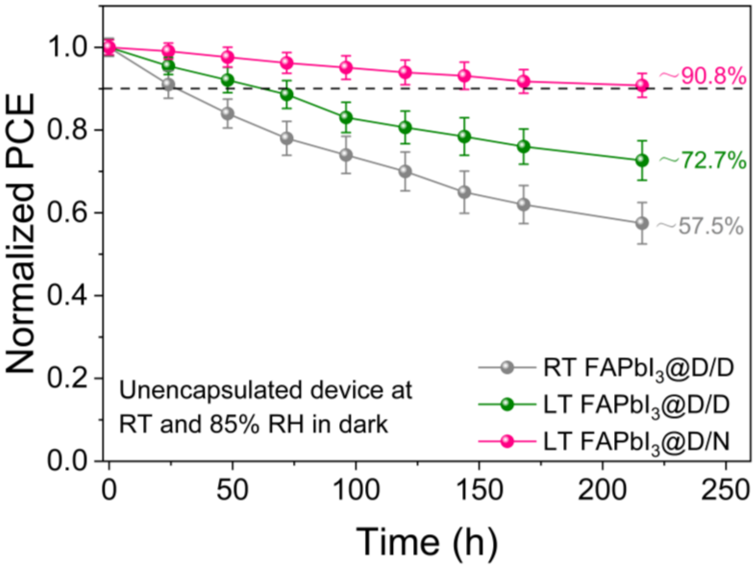

Fig. S34 Efficiency degradation tracking of the unencapsulated RT $FAPbI_3$@D/D, LT $FAPbI_3$@D/D and LT $FAPbI_3$@D/N devices under 85% relative humidity (RH) at 25 °C in a dark.

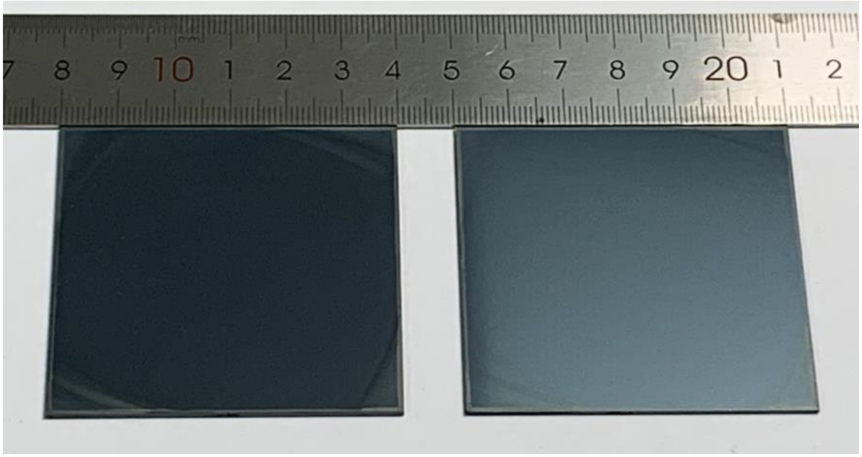

Fig. S35 Photographs of the coated 6 cm × 6 cm perovskite films. The $FAPbI_3$@D/N intermediate phase film at LT with different t_2 time (left, 0 min, right, 120 min) after 10 min annealing at 150°C.

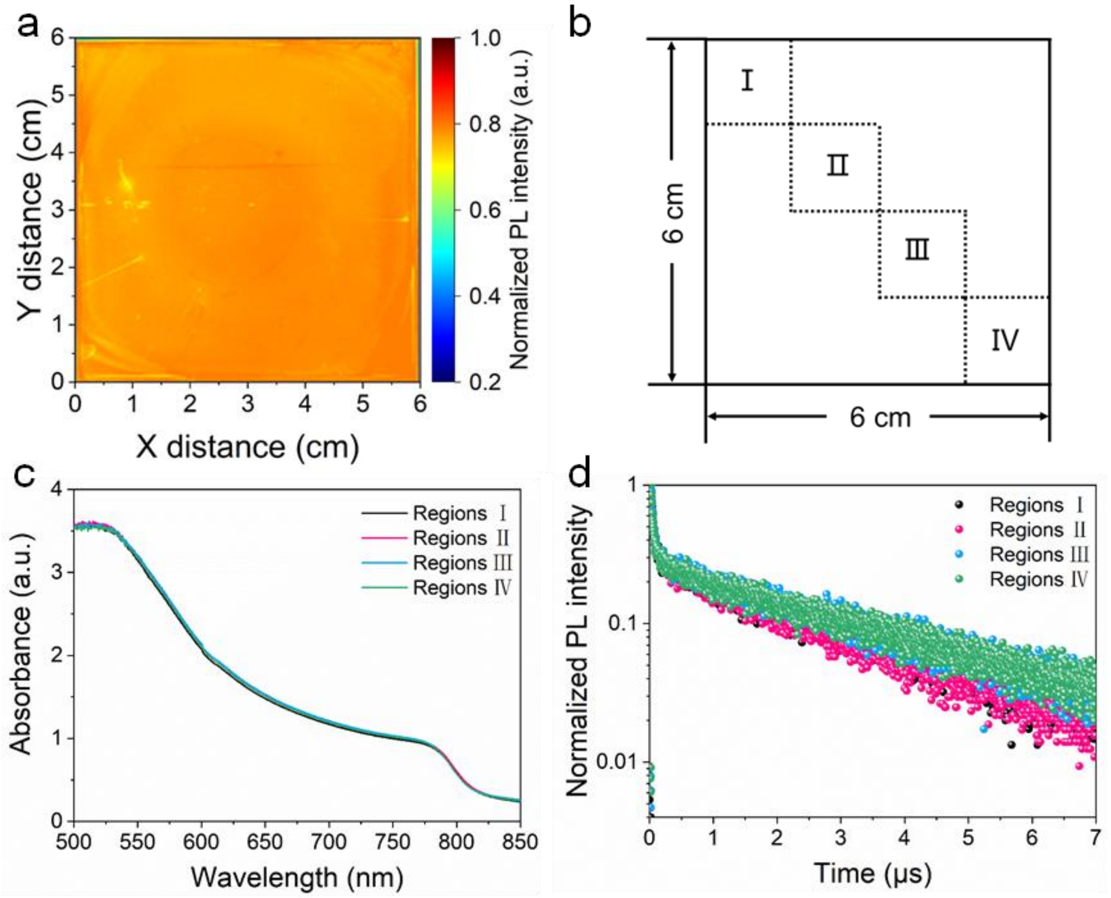

Fig. S36 Characterization of homogeneity in 6 cm × 6 cm FAPbI$_3$@D/N perovskite films prepared by the LT method (t_2=120 min). Photoelectric performance test of four typical regions of large area perovskite film: (a) PL intensity mapping profile, (b) Schematic diagram of the locations of different area, (c) UV-vis absorption spectrum, (d) TRPL spectra.

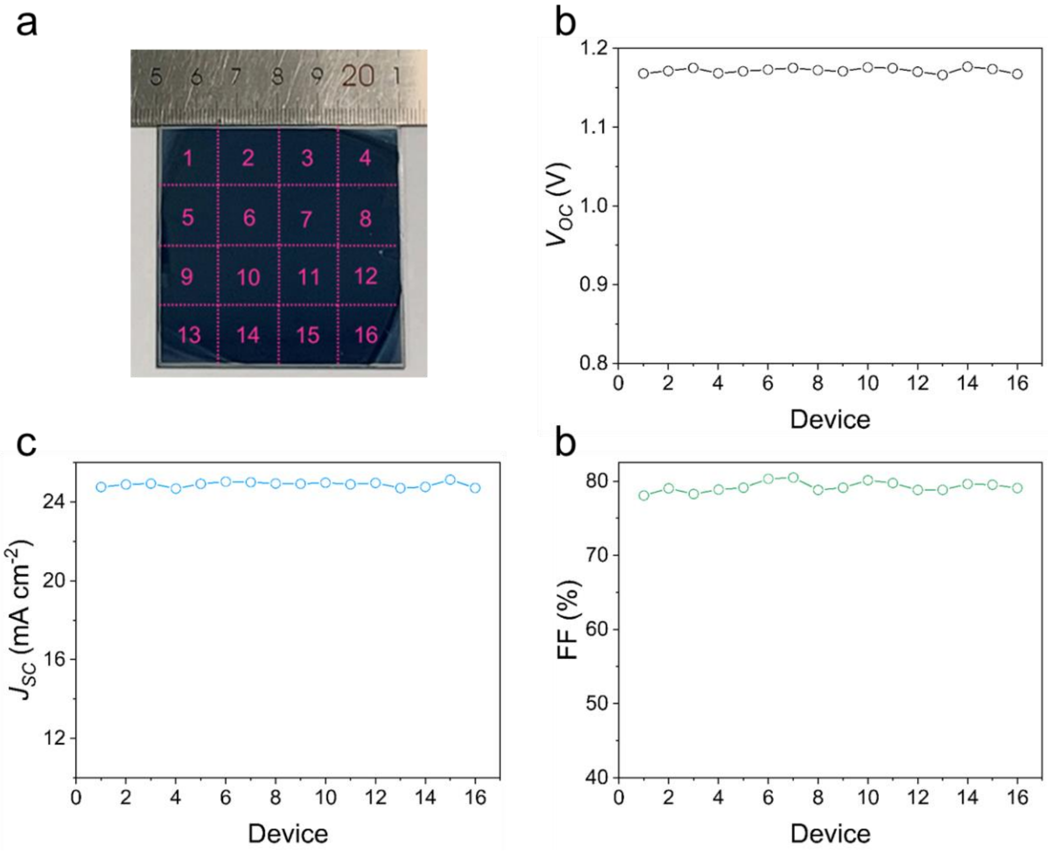

Fig. S37 (a) The image of different regions of perovskite films of 6 cm×6 cm $FAPbI_3$@D/N, and *J-V* curve performance parameters of devices derived from corresponding positions. (a) VOC, (b) JSC, (c) FF.

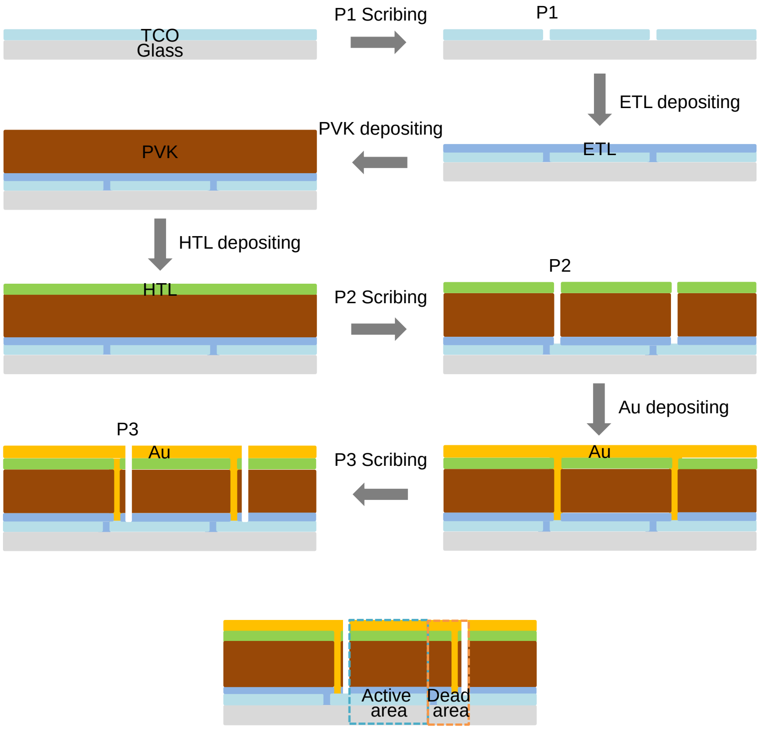

Fig. S38 Complete fabricating process of perovskite solar module. The P1 scribe separates the bottom FTO substrate, the P2 scribe provides a channel to connect the top contact of one cell to the bottom contact of the next cell to form the interconnection, and the P3 scribe isolates the top metal contact between neighboring cells. Aperture area including active area and dead area. geometric fill factor (GFF) is the ratio of active area to aperture area[30].

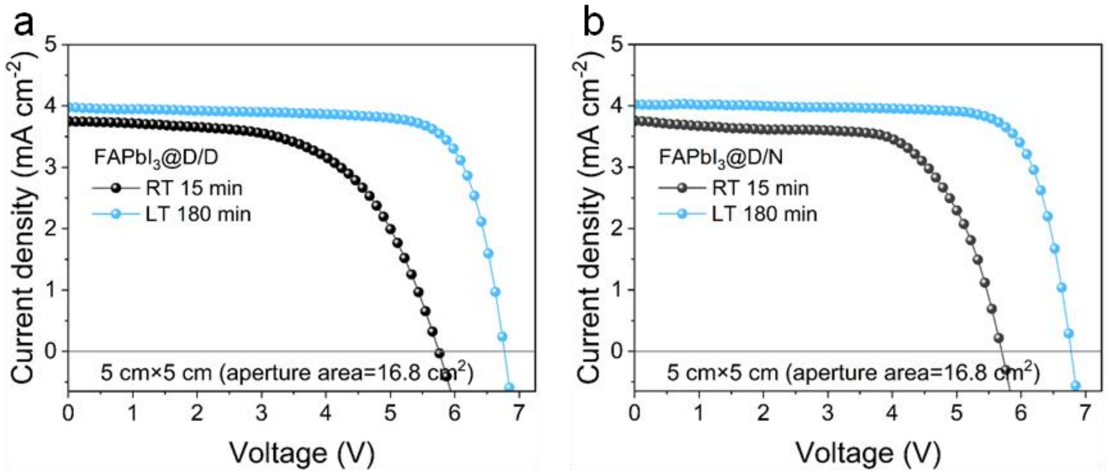

	V_{OC} (V)	J_{SC} (mA cm^{-2})	FF (%)	PCE (%)
RT 15	5.75	3.75	58.89	12.70
LT 180	6.77	3.98	76.07	20.50

	V_{OC} (V)	J_{SC} (mA cm^{-2})	FF (%)	PCE (%)
RT 15	5.70	3.76	65.62	14.06
LT 180	6.78	4.03	77.32	21.13

Fig. S39 Characterization of photovoltaic performance of 5 cm × 5 cm perovskite intermediate phases film derived modules at LT and RT with different t_2. Typical *J-V* curves of RT 15 min and LT 180 min intermediate phases film derived modules: (a) FAPbI$_3$@D/D, (b) FAPbI$_3$@D/N.

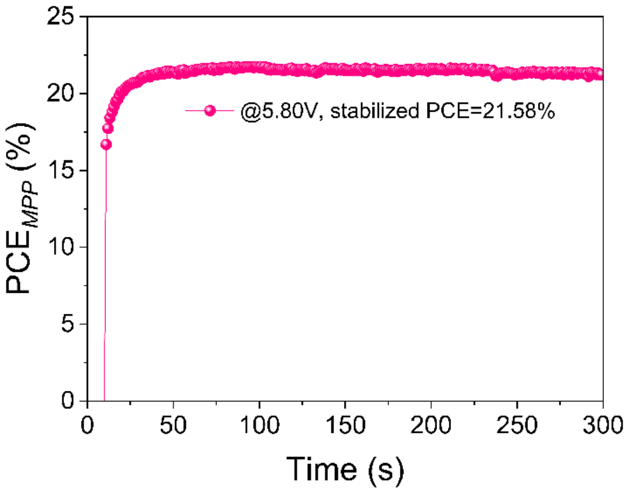

Fig. S40 The steady-state output (SPO) efficiency profiles at maximum power point for 5 cm×5 cm perovskite solar module.

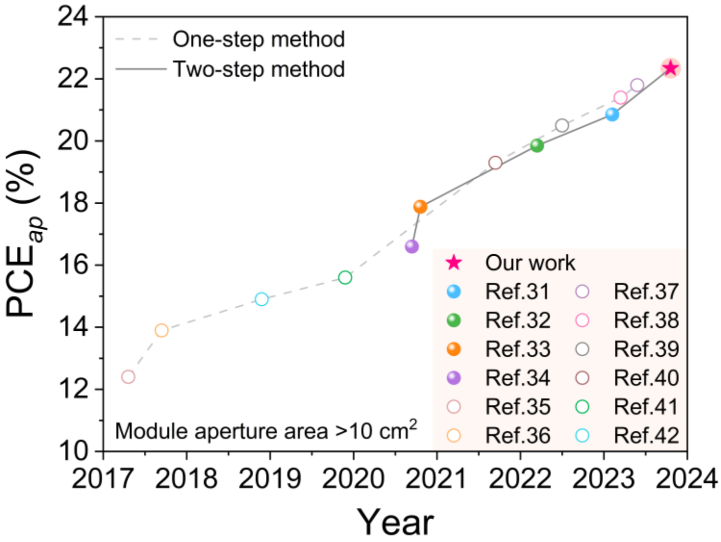

Fig. S41 Summary of publicly reported, the PCE of perovskite solar mini-modules (aperture area >10 cm^2).

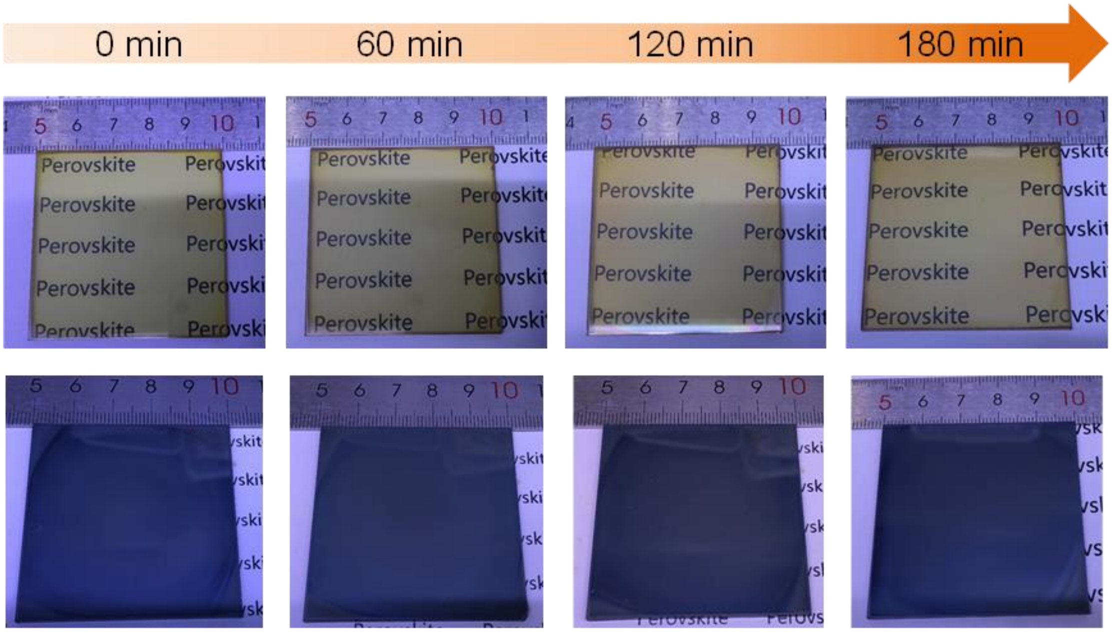

Fig. S42 Photographs of the intermediates@D/N film at LT with different t_2 and the corresponding perovskite films after 10 min annealing at 150°C.

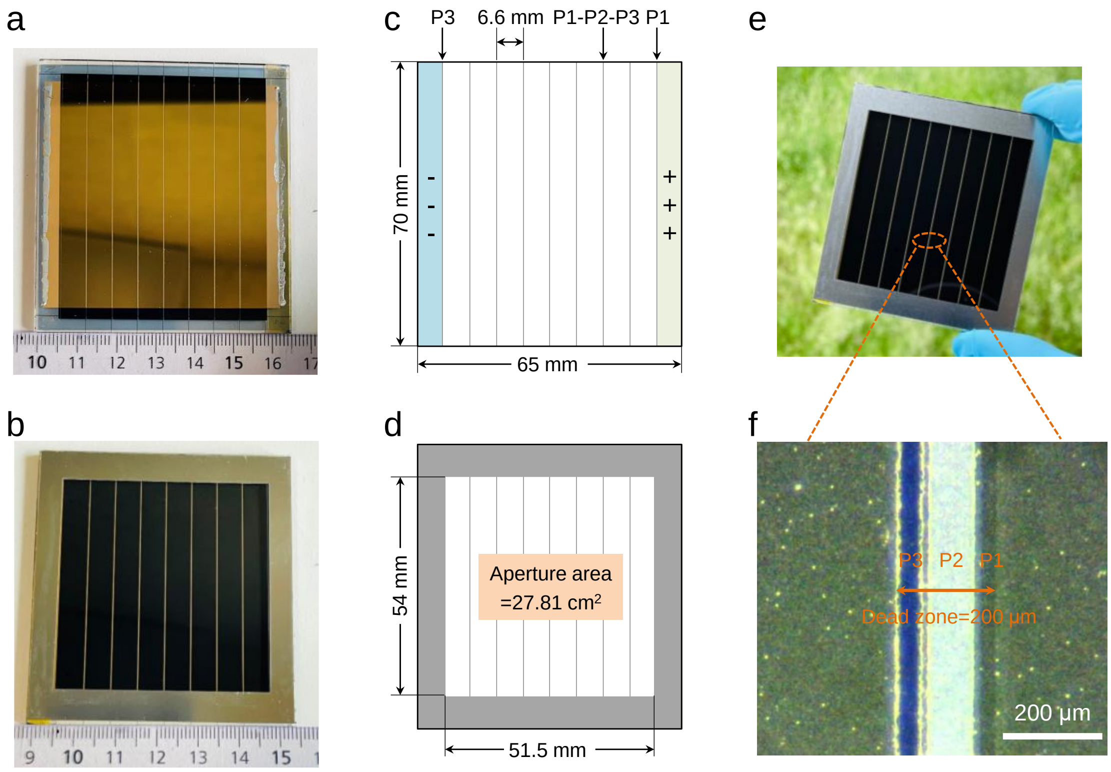

Fig. S43 Design of 6.5 cm × 7 cm perovskite solar module. (a-b) Front-side view and backside view photos of a 6.5 cm × 7 cm perovskite solar mini-module. (c) Schematic diagram of P1-P2-P3 patterning for the 6.5 cm × 7 cm module with series connection of 8-sub cells. The width of a single sub-cell is 6.6 mm. (d) The I-V test uses a 5.4 cm × 5.15 cm metal mask with an aperture area of 27.81 cm^2. (e to f) Optical photo of scribing for sub-cell separation in 6.5 cm × 7 cm perovskite solar module. P1 was scribing with a red light (532 nm) laser with a line width of about 40 µm, while P2 and P3 were scribing with a green light (1064 nm) laser with a line width of 110 µm and P3 with a line width of 50 µm. GFF = (6600 µm - 200 µm)/6600 µm =97.0%.

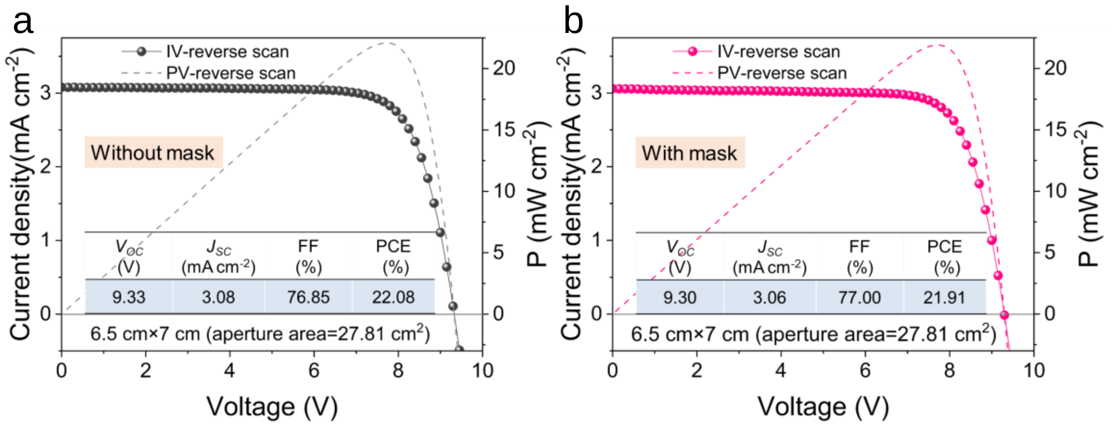

Fig. S44 The effect of metal mask on the results of 6.5 cm × 7 cm module photovoltaic performance test. (a) Without mask. (b) With mask. There are a few errors in the process of laser scribing and electrode evaporation, resulting in inaccurate calculation of the device area, which affects the test results. All *J*-*V* data in the experiment were tested using metal mask.

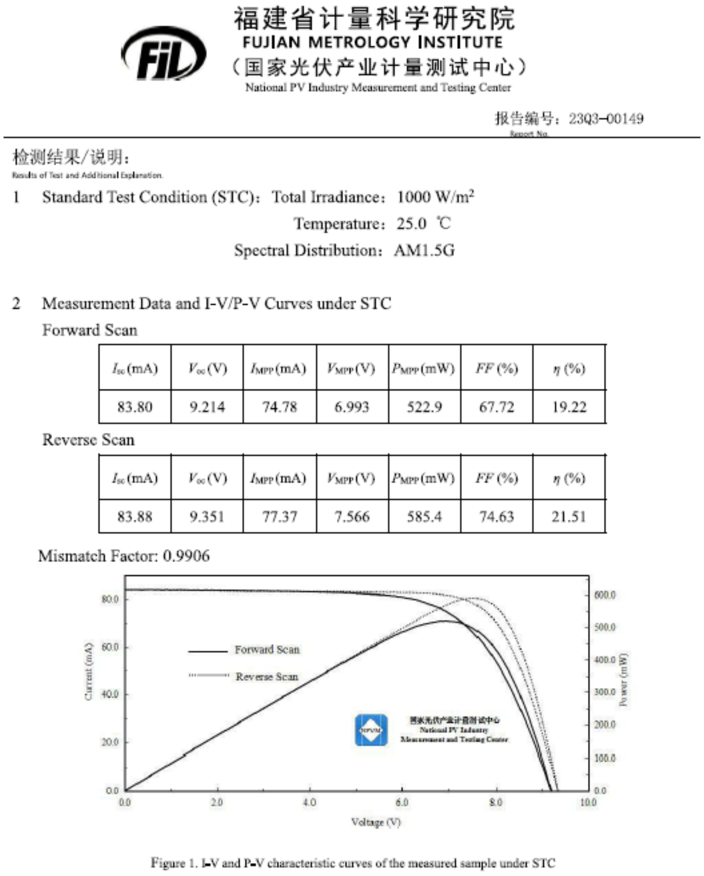

福建省计量科学研究院
FUJIAN METROLOGY INSTITUTE
（国家光伏产业计量测试中心）
National PV Industry Measurement and Testing Center

报告编号：23Q3–00149
Report No.

检测结果/说明：
Results of Test and Additional Explanation

1 Standard Test Condition (STC)：Total Irradiance：1000 W/m^2
Temperature：25.0 ℃
Spectral Distribution：AM1.5G

2 Measurement Data and I-V/P-V Curves under STC

Forward Scan

I_{sc} (mA)	V_{oc} (V)	I_{MPP} (mA)	V_{MPP} (V)	P_{MPP} (mW)	FF (%)	η (%)
83.80	9.214	74.78	6.993	522.9	67.72	19.22

Reverse Scan

I_{sc} (mA)	V_{oc} (V)	I_{MPP} (mA)	V_{MPP} (V)	P_{MPP} (mW)	FF (%)	η (%)
83.88	9.351	77.37	7.566	585.4	74.63	21.51

Mismatch Factor: 0.9906

Figure 1. I-V and P-V characteristic curves of the measured sample under STC

Fig. S45 The certified efficiency of FA-based perovskite solar module with an aperture area of 27.21 cm^2 from National PV Industry Measurement and Testing Center (NPVM), Fuzhou, China.

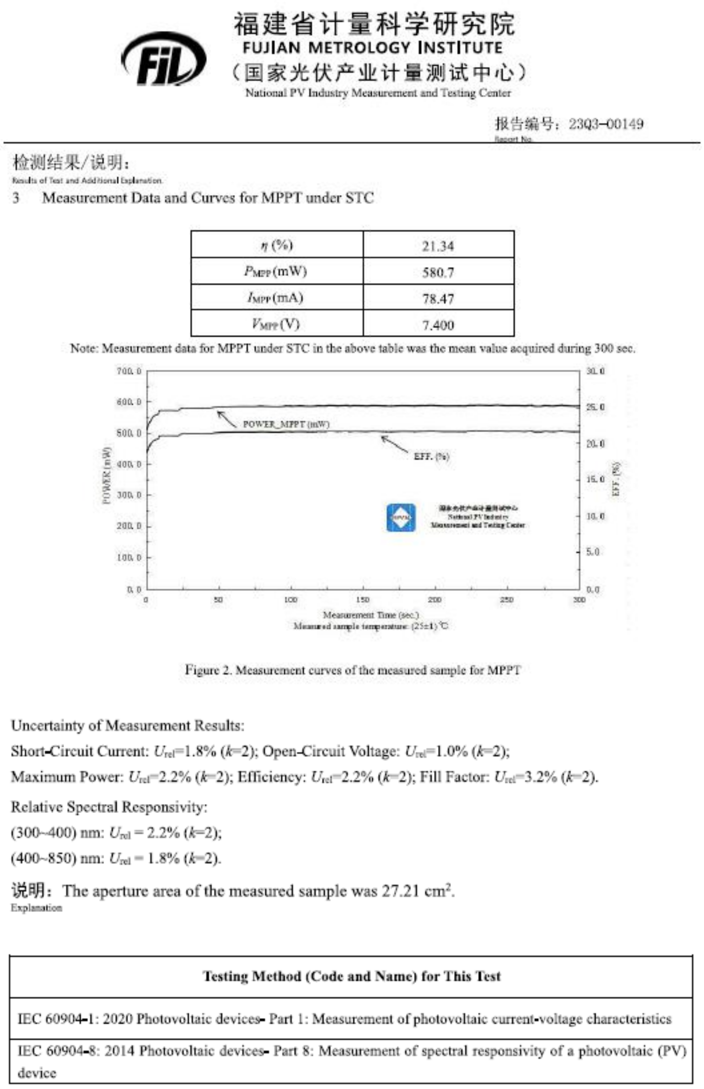

福建省计量科学研究院
FUJIAN METROLOGY INSTITUTE
（国家光伏产业计量测试中心）
National PV Industry Measurement and Testing Center

报告编号：23Q3-00149
Report No.

检测结果/说明：
Results of Test and Additional Explanation

3 Measurement Data and Curves for MPPT under STC

η (%)	21.34
P_{MPP} (mW)	580.7
I_{MPP} (mA)	78.47
V_{MPP} (V)	7.400

Note: Measurement data for MPPT under STC in the above table was the mean value acquired during 300 sec.

Figure 2. Measurement curves of the measured sample for MPPT

Uncertainty of Measurement Results:
Short-Circuit Current: U_{rel}=1.8% (k=2); Open-Circuit Voltage: U_{rel}=1.0% (k=2);
Maximum Power: U_{rel}=2.2% (k=2); Efficiency: U_{rel}=2.2% (k=2); Fill Factor: U_{rel}=3.2% (k=2).

Relative Spectral Responsivity:
(300–400) nm: U_{rel} = 2.2% (k=2);
(400–850) nm: U_{rel} = 1.8% (k=2).

说明：The aperture area of the measured sample was 27.21 cm^2.
Explanation

Testing Method (Code and Name) for This Test
IEC 60904-1: 2020 Photovoltaic devices- Part 1: Measurement of photovoltaic current-voltage characteristics
IEC 60904-8: 2014 Photovoltaic devices- Part 8: Measurement of spectral responsivity of a photovoltaic (PV) device

Fig. S46 Certification of the FA-based perovskite module with an aperture area of 27.21 cm^2 measured by maximum power point tracking by NPVM, Fuzhou, China.

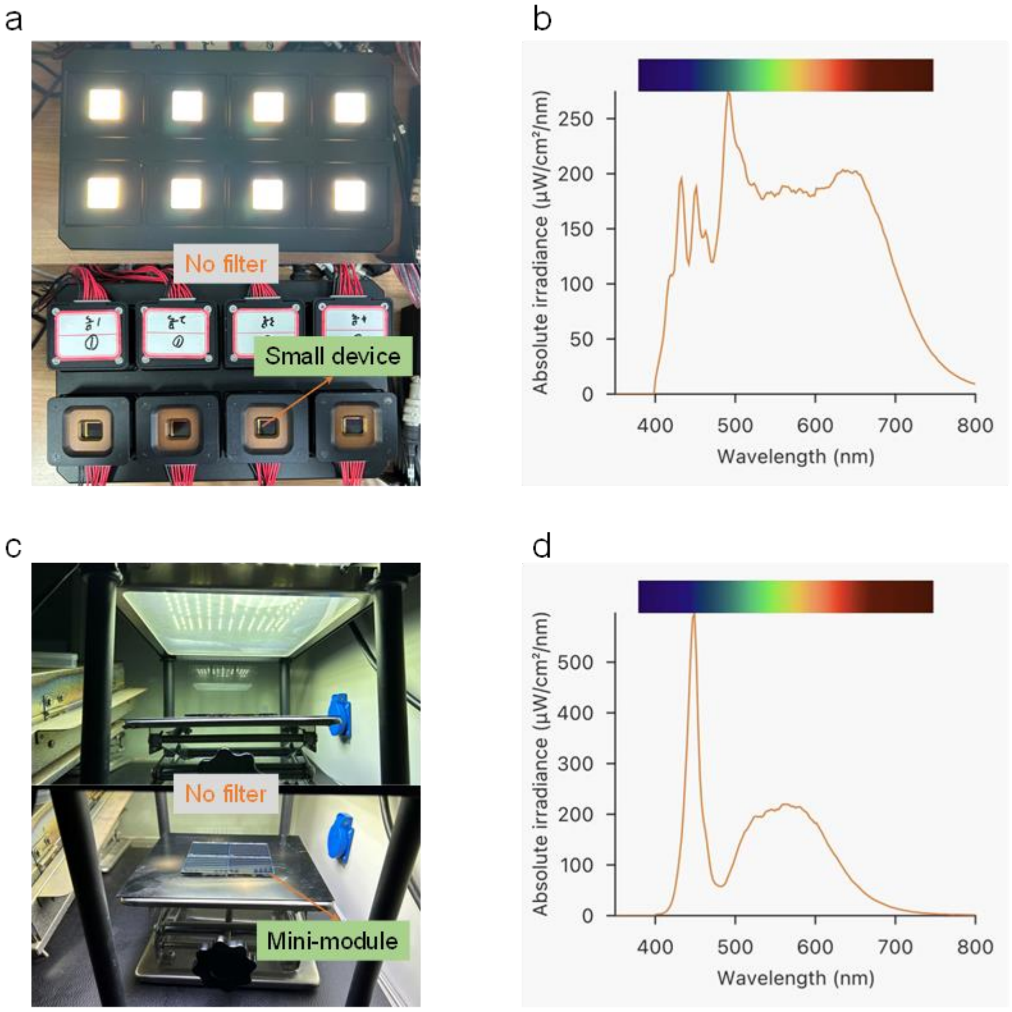

Fig. S47 (a), (c) Photographs of different light sources for light-soaking stability study. (b), (d) Light spectrum of the corresponding light sources.

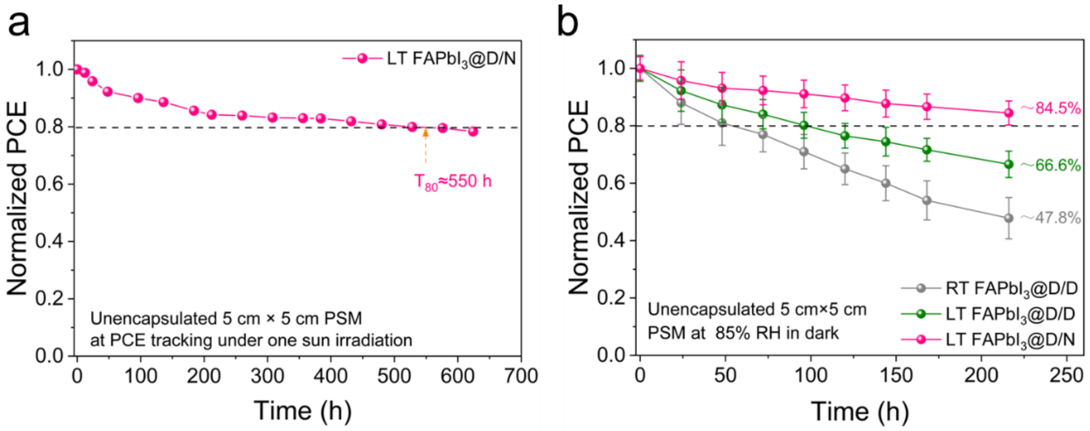

Fig. S48 Light-soaking stability and humidity stability of 5 cm × 5 cm module.

Fig. S49 Simple lighting platform for outdoor stability testing of encapsulated modules. (a) Photo of outdoor light test platform. The platform tilts at an angle of approximately 40° and faces due south. The temperature and humidity are tracked in real time by the high precision temperature and humidity recorder (COS-04), which is powered by the silicon battery charging bank. (b) Photos of outdoor illumination of modules in different weather and corresponding sunlight spectrum.

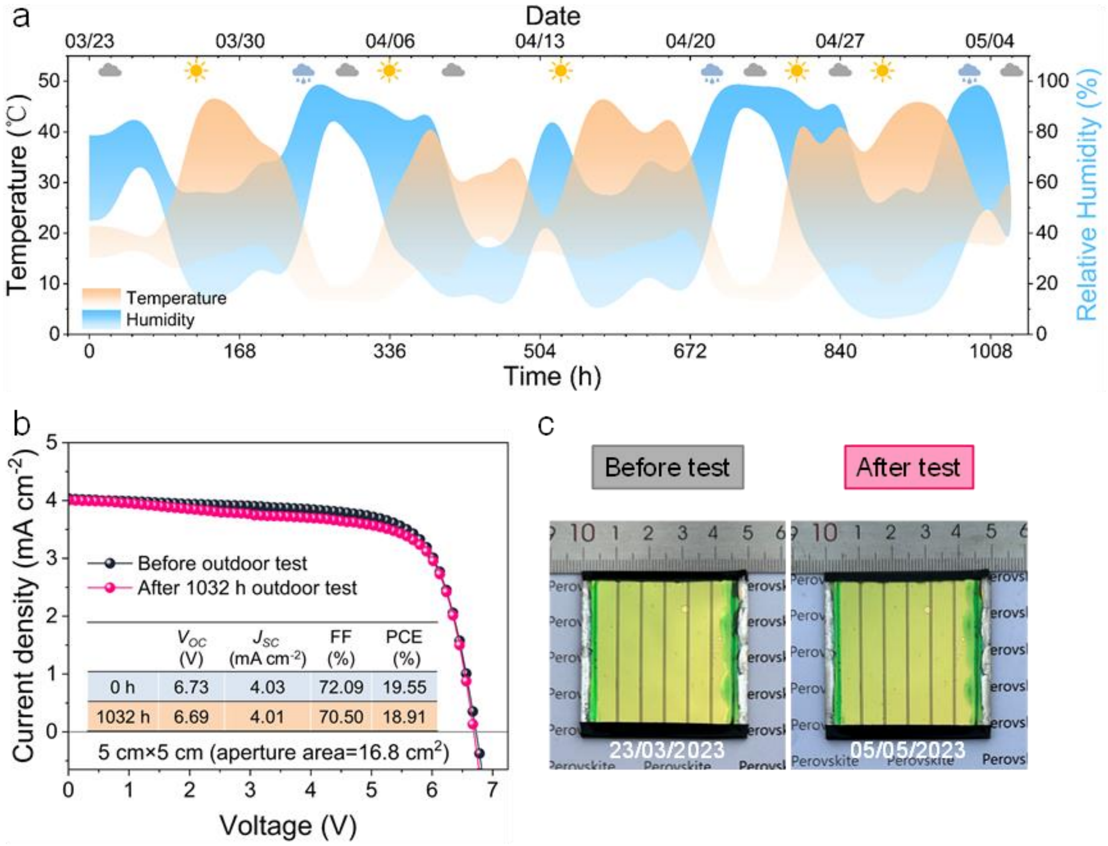

	V_{OC} (V)	J_{SC} (mA cm^{-2})	FF (%)	PCE (%)
0 h	6.73	4.03	72.09	19.55
1032 h	6.69	4.01	70.50	18.91

Fig. S50 Outdoor stability characterization of 5 cm × 5 cm perovskite modules. (a) Tracking the temperature and humidity of the outdoor ambient. (b) Corresponding *J-V* curves before and after outdoor stability test and (c) photos of encapsulated modules.

Table S1. Properties of typical solvents and additive used in the perovskite precursor inks. Density, boiling point, vapor pressure and Donor number (DN)[35,43].

Solvent	Density ($g\ cm^{-3}$)	Boiling Point (°C)	Vapor Pressure (mmHg, 20ºC)	Donor number ($kcal\ mol^{-1}$)
DMF	0.948	152-154	2.7	26.6
DMSO	1.100	189	0.42	29.8
NMP	1.028	202-204	0.29	27.3

Table S2. The kinetic process of the reaction was calculated. Potential energy (ΔE) and reaction jenthalpy (ΔH) of transition from different intermediate phases to α-$FAPbI_3$ phase and δ-$FAPbI_3$ phase.

Intermediate phases	α-$FAPbI_3$		δ-$FAPbI_3$	
	ΔE (eV)	ΔH (eV)	ΔE (eV)	ΔH (eV)
$FA_2Pb_3I_8$·4DMF	0.12	0.02	0.41	-0.15
$FAPbI_3$·2DMF	0.36	0.05	0.10	-0.12
PbI_2·2DMSO + $FA_xMA_{2-x}Pb_3I_8$·2DMSO	0.18	0.11	0.29	-0.07
(FA···NMP)PbI_3	0.13	-0.06	0.49	-0.24

Note：The kinetic process of the reaction was calculated. Positive values represent endothermic reactions and negative values exothermic reactions. For the D/D solvent system, PbI_2 can form different adducts with solvent molecules, although after annealing at 70°C in the first step, only a small amount of PbI_2•DMF adducts exist during the second step and FAI reaction (due to the decomposition temperature of PbI_2•DMF is lower than PbI_2•DMSO and PbI_2•NMP). But here we consider all the PbI_2 adducts, which will react with FAI as follows:

$2FAI + 4PbI_2{\bullet}DMF \rightarrow FA_2Pb_3I_8{\bullet}4DMF + PbI_2$ $\Delta H=0.09$ eV

$FAI + PbI_2{\bullet}2DMF \rightarrow FAPbI_3{\bullet}2DMF$ $\Delta H=0.03$ eV

$xFAI + (2-x)MAI + 4PbI_2{\bullet}DMSO \rightarrow FA_xMA_{2-x}Pb_3I_8{\bullet}2DMSO + PbI_2{\bullet}2DMSO$

$\Delta H=-6.80$ eV

The exothermic reaction occurs preferentially, so the $FAPbI_3$@D/D intermediate phase obtained in the second stage is mainly composed of PbI_2•2DMSO, $MA_2Pb_3I_8$•2DMSO and $FAPbI_3$•2DMF. The intermediate phase tends to be converted into δ-$FAPbI_3$ perovskite by theoretical calculation, which is in good agreement with *In-situ* GIWAXS pattern (Fig. 2f).

Similarly, for the D/N solvent system, different PbI_2 adducts are also considered in the second step:

$FAI + 4PbI_2{\bullet}0.5DMF0.5NMP \rightarrow FAPbI_3{\bullet}2DMF + 2PbI_2{\bullet}NMP + PbI_2 \quad \Delta H=0.16\ eV$

$2FAI + 8PbI_2{\bullet}0.5DMF0.5NMP \rightarrow FA_2Pb_3I_8{\bullet}4DMF + 4PbI_2{\bullet}NMP + PbI_2$

$\Delta H=0.11\ eV$

$FAI + PbI_2{\bullet}NMP \rightarrow (FAI\cdots NMP)PbI_3 \quad \Delta H=-3.45\ eV$

It can be seen that $FAPbI_3$@D/N intermediate phase is mainly composed of $(FAI\cdots NMP)PbI_3$ phase, and is easily transformed into α-$FAPbI_3$ perovskite.

Table S3. Summary of the detailed photovoltaic parameters. Photovoltaic parameters derived from the *J-V* curves of the small-area (0.045 cm^2) devices by different spin-coated perovskite films.

0.045 cm^2	V_{OC} (V)	J_{SC} (mA cm^{-2})	FF (%)	PCE (%)	HI
RT $FAPbI_3$@D/D-R	1.152	25.23	80.71	23.46	0.050
RT $FAPbI_3$@D/D-F	1.140	25.15	77.72	22.28	
LT $FAPbI_3$@D/D-R	1.156	25.29	80.99	23.68	0.035
LT $FAPbI_3$@D/D-F	1.143	25.20	79.33	22.85	
RT $FAPbI_3$@D/N-R	1.197	25.65	81.43	25.00	0.042
RT $FAPbI_3$@D/N-F	1.190	25.65	78.45	23.95	
LT $FAPbI_3$@D/N-R	1.200	25.62	82.01	25.21	0.033
LT $FAPbI_3$@D/N-F	1.194	25.59	79.78	24.38	

Note: Hysteresis index (HI) =(PCE_R-PCE_F)/PCE_R.

Table S4. Summary of the detailed photovoltaic parameters. Photovoltaic parameters derived from the *J-V* curves of the large-area (1.00 cm^2) devices by different spin-coated perovskite films.

1.00 cm^2	V_{OC} (V)	J_{SC} (mA cm^{-2})	FF (%)	PCE (%)
RT FAPbI$_3$@D/D-R	1.092	25.04	73.20	20.02
RT FAPbI$_3$@D/D-F	1.073	25.07	66.29	17.83
LT FAPbI$_3$@D/D-R	1.103	24.98	76.94	21.20
LT FAPbI$_3$@D/D-F	1.091	24.95	75.18	20.46
RT FAPbI$_3$@D/N-R	1.159	25.10	79.74	23.20
RT FAPbI$_3$@D/N-F	1.141	25.08	77.26	22.11
LT FAPbI$_3$@D/N-R	1.179	25.20	79.43	23.60
LT FAPbI$_3$@D/N-F	1.170	25.12	77.25	22.70

Table S5. Fitted parameters of the TRPL results. TRPL fitting results obtained using the bi-exponential decay equation $I(t) = I_0 + A_1\exp(-t/\tau_1) + A_2\exp(-t/\tau_1)$, in which A_1 and τ_1 are the amplitude and time constant for the fast decay component, respectively, and A_2 and τ_2 are the amplitude and time constant for the slow decay component, respectively. In this model, the faster decay components are attributed to defect-assisted non-radiative recombination, while the slower decay components are assigned to bimolecular radiative recombination in the bulk[44]. The average lifetime can be calculated with the equation of: $\tau_{avg} = (A_1\tau_1^2 + A_2\tau_2^2)/(A_1\tau_1 + A_2\tau_2)$.

Perovskite film	τ_1 (ns)	A_1 (%)	τ_2 (ns)	A_2 (%)	τ_{avg} (ns)
$FAPbI_3$@D/D	248.20	18.99	912.85	81.01	605.08
$FAPbI_3$@D/N	490.06	4.32	1992.07	95.68	1706.67

Table S6. Summary of the detailed photovoltaic parameters. Photovoltaic parameters derived from the *J-V* curves of the 5 cm × 5 cm perovskite solar modules with t_2=0-180 min at LT.

Device	V_{OC} (V)	J_{SC} (mA cm^{-2})	FF (%)	PCE_{ap} (%)
1	7.05	4.04	77.50	22.07
2	6.87	4.03	76.30	21.12
3	6.75	3.98	75.66	20.33
4	6.76	4.06	77.83	21.36
5	6.94	4.00	74.85	20.78
6	6.61	4.04	74.87	19.99
7	7.04	4.05	77.16	22.00
8	6.73	4.03	76.38	20.72
9	6.87	4.06	78.55	21.91
10	6.60	4.05	74.32	19.87
11	6.91	4.02	74.56	20.71
12	6.90	4.04	79.25	22.09
13	6.73	4.00	76.98	20.72
14	6.78	3.98	74.12	20.00
15	7.01	4.02	76.40	21.53
16	6.76	4.05	78.67	21.54
17	6.77	3.98	74.05	19.95
18	6.81	4.04	74.34	20.45
19	6.70	4.02	77.57	20.89

20	6.82	4.05	77.26	21.34
21	6.70	4.01	76.03	20.43
22	6.87	4.02	75.68	20.90
23	7.01	4.03	77.67	21.94
24	6.88	4.01	74.94	20.68
25	6.68	3.97	73.94	19.61
26	6.70	4.04	75.89	20.54
27	6.82	4.05	76.55	21.14
28	6.70	4.01	75.37	20.25
29	6.69	4.01	75.04	20.13
30	6.81	4.05	77.12	21.27
Average	6.81±0.12	4.02±0.02	76.19±1.47	20.88±0.70

References

S1. Q. Jiang, Y. Zhao, X. W. Zhang, X. L. Yang, Y. Chen, Z. M Chu, Q. F. Ye, X. X. Li, Z. G. Yin, J. B. You, Surface passivation of perovskite film for efficient solar cells. Nat. Photonics, 2019, 13, 500.

S2. C. Luo, G. H. J. Zheng, F. Gao, X. J. Wang, Y. Zhao, X. Y. Gao, Q. Zhao, Facet orientation tailoring via 2D-seed- induced growth enables highly efficient and stable perovskite solar cells. Joule, 2022, 6, 240-257.

S3. Y. Zha, F. Ma, Z. H. Qu, S. Q. Yu, T. Shen, H. X. Deng, X. B. Chu, X. X. Peng, Y. B. Yuan, X. W. Zhang, J. B. You, Inactive (PbI2)2RbCl stabilizes perovskite films for efficient solar cells. Science, 2022, 377, 531-534.

S4. N. X. Li, X. X. Niu, L. Li, H. Wang, Z. J. Huang, Y. Zhang, Y. H. Chen, X. Zhang, C. Zhu, H. C. Zai, Y. Ba, S. Ma, H. F. Liu, X. X. Liu, Z. Y. Guo, G. L. Liu, R. D Fan, H. Chen, J. P. Wang, Y. Z. Lun, X. Y. Wang, J. W. Hong, H. P. Xie, D. S. Jakob, X. J. G. Xu, Q. Chen, H. P. Zhou. Liquid medium annealing for fabricating durable perovskite solar cells with improved reproducibility. Science, 2021, 373, 561–567.

S5. W. Kohn, L. J. Sham, Self-Consistent Equations Including Exchange and Correlation Effects. Phys. Rev., 1965, 140, A1133–A1138.

S6. G. Kresse, D. Joubert, From ultrasoft pseudopotentials to the projector augmented-wave method. Phys. Rev. B., 1999, 59, 1758–1775.

S7. P. E. Blochl, Projector augmented-wave method. Phys. Rev. B. 1994, 50, 17953–17979.

S8. J. P. Perdew, K. Burke, M. Ernzerhof, Generalized Gradient Approximation Made Simple. Phys. Rev. Lett., 1996, 77, 3865–3868.

S9. S. Grimme, Semiempirical GGA-type density functional constructed with a long-range dispersion correction. J. Comput. Chem., 2006, 27, 1787–1799.

S10. G. Henkelman, climbing image nudged elastic band method for finding saddle points and minimum energy paths. J. Chem. Phys., 2000, 113, 9901–9904.

S11. G. Henkelman, H. Jónsson, Improved tangent estimate in the nudged elastic band method for finding minimum energy paths and saddle points. J. Chem. Phys., 2000, 113, 9978–9985.

S12. A. A. Petrov, I. P. Sokolova, N. A. Belich, G. S. Peters, P. V. Dorovatovs, Y, V. Zubavichus, V. N. Khrustalev, A. V. Petrov, M. Grätzel, E. A. Goodilin, A. B. Tarasov, Crystal Structure of DMF-Intermediate Phases Uncovers the Link Between $CH_3NH_3PbI_3$ Morphology and Precursor Stoichiometry. J. Phys. Chem. C., 2017, 121, 20739–20743.

S13. F. W. Cheng, X. J. Jing, R. H. Chen, J. Cao, J. Z. Yan, Y. Y. Q. Wu, X. F. Huang, B. H. Wu N. F. Zheng, N-Methyl-2-pyrrolidone as an excellent coordinative additive with a wide operating range for fabricating high-quality perovskite films. Inorg. Chem. Front., 2019, 6, 2458–2463.

S14. A. A. Petrov, S. A. Fateev, V. N. Khrustalev, Y. M. Li, P. V. Dorovatovskii, Y. V. Zubavichus, E. A. Goodilin, A. B. Tarasov, Formamidinium Haloplumbate Intermediates: The Missing Link in a Chain of Hybrid Perovskites Crystallization, Chem. Mater., 2020, 32, 7739–7745.

S15. Y. Huang, L. Li, Z. H. Liu, H. Y. Jiao, Y. Q. He, X. G. Wang, R. Zhu, D. Wang, J. L. Sun, Q. Chen, H. P. Zhou, The intrinsic properties of $FA_{(1-X)}MA_xPbI_3$ perovskite single crystals. J. Mater. Chem. A., 2017, 5, 8537–8544.

S16. C. C. Stoumpos, C. D. Malliakas, M. G. Kanatzidis, Semiconducting Tin and Lead Iodide Perovskites with Organic Cations: Phase Transitions, High Mobilities, and Near-Infrared Photoluminescent Properties. Inorg. Chem. 2013, 52, 9019–9038.

S17. A. Marronnier, G. Roma, S. Boyer-Richard, L. Pedesseau, J.-M. Jancu, Y. Bonnassieux, C. Katan, C. C. Stoumpos, M. G. Kanatzidis, J. Even, Anharmonicity and Disorder in the Black Phases of Cesium Lead Iodide Used for Stable Inorganic Perovskite Solar Cells. ACS Nano, 2018, 12, 3477–3486.

S18. T. L. Bu, J. Li, H. Y. Li, C. C. Tian, J. Su, G. Q. Tong, L. K. Ono, C. Wang, Z. P. Lin, N. Y. Chai, X.-L. Zhang, J. J. Chang, J. F. Lu, J. Zhong, W. C. Huang, Y. B. Qi, Y. -B. Cheng, F. Z. Huang, Lead halide–templated crystallization of methylamine-free perovskite for efficient photovoltaic modules. Science, 2021, 372, 1327–1332.

S19. J. Chung, S.-W. Kim, Y. Li, T. Mariam, X. M. Wang, M. Rajakaruna, M. M. Saeed, A. Abudulimu, S. S. Shin, K. N. Guye, Z. X. Huang, R. J. E. Westbrook, E. Miller, B. Subedi, N, J. Podraza, M. J. Heben, R. J. Ellingson, D. S. Ginger, Z. N. Song, Y. F. Yan, Engineering Perovskite Precursor Inks for Scalable Production of High-Efficiency Perovskite Photovoltaic Modules. Adv. Energy Mater., 2023, 13, 2300595.

S20. J. Cao, X. J. Jing, J. Z. Yan, C. Y. Hu, R. H. Chen, J. Yin, J. Li, N. F. Zheng, Identifying the Molecular Structures of Intermediates for Optimizing the Fabrication of High-Quality Perovskite Films. J. Am. Chem. Soc., 2016, 138, 9919−9926.

S21. G. L. Wang, Q. Lian, D. Wang, F. Jiang, G. J. Mi, D. Y. Li, Y. L. Huang, Y. Wang, X. Y. Yao, R. Shi, C. Liao, J. H. Zheng, A. Ho-Baillie, A. Amini, B. M. Xu, C. Cheng, Thermal-Radiation-Driven Ultrafast Crystallization of Perovskite Films Under Heavy Humidity for Efficient Inverted Solar Cells. Adv. Mater., 2022, 34, 2205143.

S22. Y. L. Guo, K. Shoyama, W. Sato, Y. Matsuo, K. Inoue, K. Harano, C. Liu, H. Tanaka, E. Nakamura, Chemical Pathways Connecting Lead(II) Iodide and Perovskite via Polymeric Plumbate(II) Fiber. J. Am. Chem. Soc., 2015, 137, 15907-15914.

S23. Y. H. Jo, K. S. Oh, M. J. Kim, K.-H. Kim, H. Lee, C. -W. Lee, D. S. Kim, High Performance of Planar Perovskite Solar Cells Produced from PbI_2(DMSO) and PbI_2(NMP) Complexes by Intramolecular Exchange. Adv. Mater. Interfaces., 2016, 3, 1500768.

S24. K. Zhang, Z. Wang, G. P. Wang, J. Wang, Y. Li, W. Qian, S. Z. Zheng, S. Xiao, S. H. Yang, A prenucleation strategy for ambient fabrication of perovskite solar cells with high device performance uniformity. Nat. Commun., 2020, 11, 1006.

S25. M. B. Li, R. M. Sun, J. X. Chang, J. J. Dong, Q. S. Tian, H. Z. Wang, Z. H. Li, P. H. Yang, H. K. Shi, C. Yang, Z. C. Wu, R. Z. Li, Y. G. Yang, A. f. Wang, S. T Zhang, F. F. Wang, W. Huang, T. S. Qin, Orientated crystallization of FA-based perovskite via hydrogen-bonded polymer network for efficient and stable solar cells. Nat. Commun., 2023, 14, 573.

S26. J.-W. Lee, Z. H. Dai, C. S. Lee, H. M. Lee, T.-H. Han, N. D. Marco, O. Lin, C. S. Choi, B. Dunn, J. Koh, D. D. Carlo, J. H. Ko, H. D. Maynard, Y. Yang, Tuning Molecular Interactions for Highly Reproducible and Efficient Formamidinium Perovskite Solar Cells via Adduct Approach. J. Am. Chem. Soc., 2018, 140, 6317−6324.

S27. H. Z. Lu, Y. H. Liu, P. Ahlawat, A. Mishra, W. R. Tress, F. T. Eickemeyer, Y. G. Yang, F. Fu, Z. W. Wang, C. E. Avalos, B. I. Carlsen, A. Agarwalla, X. Zhang, X. G. Li, Y. Q. Zhan, S. M. Zakeeruddin, L. Emsley, U. Rothlisberger, L. G. Zheng, A. Hagfeldt, M. Grätzel, Vapor-assisted deposition of highly efficient, stable black-phase $FAPbI_3$ perovskite solar cells. Science, 2020, 370, 74.

S28. Y. S. Ge, F. H. Ye, M. Xiao, H. B. Wang, C. Wang, J. W. Liang, X. Z. Hu, H. L. Guan, H. S. Cui, W. J. Ke, C. Tao, G. J. Fang, Internal Encapsulation for Lead Halide Perovskite Films for Efficient and Very Stable Solar Cells. Adv. Energy Mater, 2022, 12, 2200361.

S29. X. D. Li, W. X. Zhang, X. M. Guo, C. Y. Lu, J. Y. Wei, J. F. Fang, Constructing heterojunctions by surface sulfidation for efficient inverted perovskite solar cells. Science, 2022, 375, 434-437.

S30. M. Y. Du, X. J. Zhu, L. K. Wang, H. Wang, J. S. Feng, X. Jiang, Y. X. Cao, Y. M. Sun, L. J. Duan, Y. X. Jiao, K. Wang, X. D. Ren, Z. Yan, S. P. Pang, S. Z. (Frank) Liu, High-Pressure Nitrogen-Extraction and Effective Passivation to Attain Highest Large-Area Perovskite Solar Module Efficiency. Adv. Mater., 2020, 32, 2004979.

S31. Y. X. Shen, G. Y. Xu, J. J. Li, X. Lin, F. Yang, H. Y. Yang, W. J. Chen, Y.Y. Wu, X. X. Wu, Q. R. Cheng, J. Zhu, Y. W. Li, Y. F. Li, Functional Ionic Liquid Polymer Stabilizer for High-Performance Perovskite Photovoltaics. Angew. Chem. Int. Ed., 2023, 62, e202300690.

S32. H. Li, J. J. Zhou, L. G. Tan, M. H. Li, C. F. Jiang, S. Y. Wang, X. Zhao, Y. Liu, Y. Zhang, Y. R. Ye, W. Tress, C. Y. Yi, Sequential vacuum-evaporated perovskite solar cells with more than 24% efficiency. Sci. Adv., 2022, 8, eabo7422.

S33. A. B. Ren, H. G. Lai, X. Hao, Z. G. Tang, H. Xu, B. M. F. Y. Jeco, K. Watanabe, L. L Wu, J. Q. Zhang, M. Sugiyama, J. Wu, D. W. Zhao. Efficient Perovskite Solar Modules with Minimized Nonradiative Recombination and Local Carrier Transport Losses. Joule, 2020, 4, 1263–1277.

S34. Z. H. Liu, L. B. Qiu, L. K. Ono, S. S. He, Z. H. Hu, M. W. Jiang, G. Q. Tong, Z. F. Wu, Y. Jiang, D.-Y. Son, Y. Y. Dang, S. Kazaoui, Y. B. Qi, A holistic approach to interface stabilization for efficient perovskite solar modules with over 2,000-hour operational stability. Nat. Energy, 2020, 5, 596–604.

S35. M. J. Yang, Z. Li, M. O. Reese, O. G. Reid, D. H. Kim, S. Siol, T. R. Klein, Y. F. Yan, J. J. Berry, M. F. A. M. van Hest, K. Zhu, Perovskite ink with wide processing window for scalable high-efficiency solar cells. Nat. Energy, 2017, 2, 17038.

S36. H. Chen, F. Ye, W. T. Tang, J. J. He, M. S. Yin, Y. B. Wang, F. X. Xie, E. B. Bi, X. D. Yang, M. Grätzel, L. Y. Han, A solvent- and vacuum-free route to large-area perovskite films for efficient solar modules. Nature, 2017, 550, 92–95.

S37. C. B. Fei, N. X. Li, M. R. Wang, X. M. Wang, H. Y. Gu, B. Chen, Z. Zhang, Z. Y. Ni, H. Y. Jiao1, W. Z. Xu, Z. F. Shi, Y. F. Yan, J. S. Huang, Lead-chelating hole-transport layers for efficient and stable perovskite minimodules. Science, 2023, 380, 823–829.

S38. S. You, H. P. Zeng, Y. H. Liu, B. Han, M. Li, L. Li, X. Zheng, R. Guo, L. Luo, Z. Li, C. Zhang, R. R. Liu, Y. Zhao, S. J. Zhang, Q. Peng, T. Wang, Q. Chen, F. T. Eickemeyer, B. Carlsen, S. M. Zakeeruddin, L. Q. Mai, Y. G. Rong, M. Grätzel, X. Li, Radical polymeric p-doping and grain modulation for stable, efficient perovskite solar modules. Science, 2023, 379, 288–294.

S39. T. L. Bu, L. K. Ono, J. Li, J. Su, G. Q. Tong, W. Zhang, Y. Q. Liu, J. H. Zhang, J. J. Chang, S. Kazaoui, F. Z. Huang, Y.-B. Cheng, Y. B. Qi, Modulating crystal growth of formamidinium–caesium perovskites for over 200 cm^2 photovoltaic sub-modules. Nat. Energy, 2022, 7, 528–536.

S40. S. S. Chen, X. Z. Dai, S. Xu, H. Y. Jiao, L. Zhao, J. S. Huang, Stabilizing perovskite-substrate interfaces for high-performance perovskite modules. Science, 2021, 373, 902–907.

S41. T. Bu, J. Li, F. Zheng, W. Chen, X. Wen, Z. Ku, Y. Peng, J. Zhong, Y.-B. Cheng, F. Huang, Universal passivation strategy to slot-die printed SnO_2 for hysteresis-free efficient flexible perovskite solar module. Nat. Commun., 2018, 9, 4609.

S42. E. B. Bi, W. T. Tang, H. Chen, Y. B. Wang, J. L. Barbaud, T. H. Wu, W. Y. Kong, P. Tu, H. Zhu, X. Q. Zeng, J. J. He, S.-I. Kan, X. D. Yang, M. Grätzel, L. Y. Han, Efficient Perovskite Solar Cell Modules with High Stability Enabled by Iodide Diffusion Barriers. Joule, 2019, 3, 2748-2760.

S43. X. F. Huang, G. H. Deng, S. Q. Zhan, F. Cao, F. W. Cheng, J. Yin, J. Li, B. H. Wu, N. F. Zheng, Solvent Gaming Chemistry to Control the Quality of Halide Perovskite Thin Films for Photovoltaics. ACS Cent. Sci., 2022, 8, 1008–1016.

S44. J. Zhu, Y. T. Qian, Z. J. Li, O. Y. Gong, Z. F. An, Q. Liu, J. H. Choi, H. Guo, P. J. Yoo, D. H. Kim, T. K. Ahn, G. S. Han, H. S. Jung, Defect Healing in $FAPb(I_{1-x}Br_x)_3$ Perovskites: Multifunctional Fluorinated Sulfonate Surfactant Anchoring Enables >21% Modules with Improved Operation Stability. Adv. Energy Mater., 2022, 12, 2200632.